Analysis and Control of Current Harmonic in IPMSM Field-Oriented Control System

Zhiwei Chen, Tingna Shi, *Member, IEEE*, Zhichen Lin, Zhiqiang Wang, *Member, IEEE*, and Xin Gu, *Member, IEEE*

***Abstract*—There is a certain amount of current harmonics in interior permanent magnet synchronous motor. In order to accurately control the current harmonic, this article focuses on three aspects: establishing current harmonic calculation model, extracting current harmonic, and designing current harmonic regulator. A current harmonic calculation model, which considers the effect of voltage harmonics induced by current controllers and digital control delay on the initial phase angle of voltage harmonics, is established for the first time. With the help of multiple synchronous rotating frame transformation, a current harmonic extraction method more suitable for motor drive field, which aims to extract the current harmonic characteristics of *d*-axis and *q*-axis currents, is proposed. On this basis, the controlled quantity and control quantity are unified in *d–q* coordinate frame for analyzing the coupling relationship of current harmonic characteristics. And then a PI current harmonic regulator, including current harmonic decoupling and voltage harmonic initial phase angle compensation, is constructed, so as to realize the effective control of current harmonics. Finally, the effectiveness and superiority of the proposed method are verified by simulation and experiments.**

***Index Terms*—Current harmonics analysis, current harmonics regulator, field-oriented control, interior permanent magnet synchronous motor (IPMSM), PI.**

I. Introduction

INTERIOR permanent magnet synchronous motor (IPMSM) is widely used in electric vehicle drive system because of its compact structure and high power density. During actual operation, the dead time of inverter and nonsinusoidal flux linkage of permanent magnet will deteriorate the operation quality of motor [1]. When the permanent magnet flux linkage is sinusoidal, the current harmonic is controlled to zero, which will effectively reduce the motor loss and torque ripple [5]. When the flux linkage of permanent magnet is nonsinusoidal, it is necessary to ensure a certain amount of current harmonics to reduce torque ripple [1]. Therefore, how to control the current harmonic to achieve the desired value is of great significance for current harmonic suppression or torque ripple suppression.

The essence of controlling current harmonics is to inject a certain amount of voltage harmonics into the motor control system to make the current harmonics meet the reference. In order to control current harmonics, on the one hand, it is necessary to obtain the current harmonic of certain order in the motor system accurately. On the other hand, it is necessary to design a current harmonic regulator with good performance. Fully understanding the relationship between current harmonic and voltage harmonic has a good guiding significance for the design of current harmonic regulator.

As we all know, dead time of inverter and motor permanent magnet flux harmonic are the two main sources of voltage harmonics in motor system. And those make the phase current of the motor contains the corresponding current harmonic. In this regard, many scholars have conducted relevant research and obtained the current harmonic calculation formula for the motor [3]–[8]. However, in motor control system, the motor current containing a certain harmonic will be fed back to the *d*-axis and *q*-axis current controllers, which will also induce a certain voltage harmonic. Therefore, in order to accurately obtain the current harmonic calculation model in the field-oriented control (FOC) system, the influence mechanism of voltage harmonic output by *d*-axis and *q*-axis current controllers on current harmonic needs to be deeply studied.

In terms of current harmonic extraction, some scholars use filters to extract current harmonics, such as band-pass filter and adaptive filter based on least mean square [8]–[10]. Adaptive linear neurons also can be used to extract current harmonics [5]. All the aforementioned methods aim to obtain the current harmonics in the form of ac. In recent years, the multiple synchronous rotating frame transformation (MSRFT) method, which is widely used in power system and aimed at extracting the dc characteristic quantities of current harmonics, has attracted extensive attention [12]–[15]. In these methods, the three-phase currents are usually transformed into a combination of a dc component corresponding to the current harmonic of a certain frequency and several ac components through MSRFT, and then combined with the first-order low-pass filter (FLPF) to realize the extraction of current harmonic characteristic quantities in

Manuscript received September 7, 2021; revised January 8, 2022; accepted February 24, 2022. Date of publication March 1, 2022; date of current version April 28, 2022. This work was supported in part by the National Natural Science Foundation of China under Grant 51977150 and in part by the Tianjin Natural Science Foundation under Grant 19JCYBJC21800. Recommended for publication by Associate Editor U. Deshpande. *(Corresponding author: Tingna Shi.)*

Zhiwei Chen is with the School of Electrical and Information Engineering, Tianjin University, Tianjin 300072, China (e-mail: chenzw@tju.edu.cn).

Tingna Shi and Zhichen Lin are with the College of Electrical Engineering, Zhejiang University, Hangzhou 310027, China, and also with the Zhejiang University Advanced Electrical Equipment Innovation Center, Hangzhou 311107, China (e-mail: tnshi@zju.edu.cn; linzhichen@zju.edu.cn).

Zhiqiang Wang and Xin Gu are with the School of Electrical Engineering, Tiangong University, Tianjin 300387, China (e-mail: wangzhiqiang@tiangong.edu.cn; guxin@tiangong.edu.cn).

Color versions of one or more figures in this article are available at https://doi.org/10.1109/TPEL.2022.3155243.

Digital Object Identifier 10.1109/TPEL.2022.3155243

the phase current. Because the attenuation of FLPF to the signal at the cutoff frequency will not be zero, especially for high current amplitude, it is difficult to completely eliminate the ac amount corresponding to the fundamental current in the phase current, which will affect the extraction of characteristic quantities. This is the reason why the current harmonic extraction method based on MSRFT is difficult to be effectively applied to motor control system. In this regard, many scholars try to improve the application performance of MSRFT in the field of motor control, and have made some progress. The method of FLPF with closed-loop feedback is adopted in [2]. Second-order Butterworth filter and type II Chebyshev filter are adopted in [14] and [15]. These methods improve the accuracy of current harmonic characteristic quantities extraction. But they increase the complexity of the algorithm to a certain extent. So, strategies to ensure the accuracy of current harmonic characteristic quantities extraction without increasing the complexity need to be further studied.

In terms of current harmonic regulator design, current harmonic regulators based on repetitive controller, iterative learning controller, and proportional resonance controller have been proposed successively [16]–[19]. These kind of regulator can control the current harmonic. However, the parameters of regulator often need to be adjusted with harmonic frequency. PI current harmonic regulator, which direct controls the dc variables, can avoid this problem [13]–[15]. In the existing PI current harmonic regulator, the extracted current harmonic characteristic quantities in three-phase coordinate frame are usually passed through PI to generate the desired voltage harmonic characteristic quantities, and then the results are injected into the control system through inverse MSRFT (IMSRFT), so as to realize the control of current harmonics. However, through research, we find that due to the lack of accurate understanding of the mathematical relationship between current harmonic and voltage harmonic in motor-field-oriented control system, the existing schemes often control current harmonic harder and less effective.

In view of this, how to accurately establish current harmonic calculation model, improve the application performance of MSRFT in motor control system, and design PI current harmonic regulator are studied in this article. First, the influence of voltage harmonics generated by *d*-axis and *q*-axis current controllers on current harmonics in field-oriented control system is fully considered, and the influence of digital control delay on the initial phase angle of voltage harmonics output by current controllers is analyzed for the first time. Based on this, the calculation model of *d*-axis and *q*-axis current harmonics is derived. Then, the current harmonic extraction method based on MSRFT is improved to accurately extract *d*-axis and *q*-axis current harmonic characteristic quantities. Finally, according to the relationship between *d*-axis, *q*-axis current harmonics and voltage harmonics established, a PI current harmonic regulator based on unified coordinate frame, which adds two parts: current harmonic decoupling and voltage harmonic initial phase angle compensation, is designed. The effectiveness and superiority of the proposed method are verified by simulation and experiments.

II. Current Harmonics Calculation Considering the Influence of Voltage Harmonics Output by Current Controllers and Digital Control Delay

A. Mathematical Model of Current Loop in FOC System

In the *d–q* synchronous frame, the generalized IPMSM stator voltage equation, which considers the voltage harmonic induced by permanent magnet harmonic and dead time of the inverter, can be expressed as

$$\begin{cases} v_{\mathrm{d\_m}} = Ri_{\mathrm{d}} + L_{\mathrm{d}}\mathrm{p}i_{\mathrm{d}} - \omega_{\mathrm{e}}L_{\mathrm{q}}i_{\mathrm{q}} + \mathrm{p}\lambda_{\mathrm{d}} - \omega_{\mathrm{e}}\lambda_{\mathrm{q}} + \Delta v_{\mathrm{d\_}z} \\ v_{\mathrm{q\_m}} = Ri_{\mathrm{q}} + L_{\mathrm{q}}\mathrm{p}i_{\mathrm{q}} + \omega_{\mathrm{e}}L_{\mathrm{d}}i_{\mathrm{d}} + \mathrm{p}\lambda_{\mathrm{q}} + \omega_{\mathrm{e}}\lambda_{\mathrm{d}} + \Delta v_{\mathrm{q\_}z} \end{cases} \tag{1}$$

where $v_{\mathrm{d\_m}}$ and $v_{\mathrm{q\_m}}$ are the stator voltages in *d–q* frame; *R* is the stator resistance; i_{d} and i_{q} are the currents in *d–q* frame; L_{d} and L_{q} represent the *d*-axis stator inductance and *q*-axis stator inductance, respectively; λ_{d} and λ_{q} are the flux linkages of the permanent magnet; ω_{e} is the electrical angular velocity; $\Delta v_{\mathrm{d\_z}}$ and $\Delta v_{\mathrm{q\_z}}$ represent the voltage harmonics induced by dead time of the inverter; p is the differential symbol.

In (1), the stator voltages, the *d*-axis, *q*-axis currents, permanent magnet flux linkage, and the voltage harmonics induced by inverter dead time can be expressed as

$$\begin{cases} v_{\mathrm{d\_m}} = v_{\mathrm{d0\_m}} \\ +\sum v_{\mathrm{d}k\_\mathrm{m}} = v_{\mathrm{d0\_m}} + \sum V_{\mathrm{d}k\_\mathrm{m}}\cos(k\omega_{\mathrm{e}}t + \phi_{\mathrm{d}k\_\mathrm{m}}) \\ v_{\mathrm{q\_m}} = v_{\mathrm{q0\_m}} \\ +\sum v_{\mathrm{q}k\_\mathrm{m}} = v_{\mathrm{q0\_m}} + \sum V_{\mathrm{q}k\_\mathrm{m}}\sin(k\omega_{\mathrm{e}}t + \phi_{\mathrm{q}k\_\mathrm{m}}) \end{cases} \tag{2}$$

$$\begin{cases} i_{\mathrm{d}} = i_{\mathrm{d0}} + \sum i_{\mathrm{d}k} = i_{\mathrm{d0}} + \sum I_{\mathrm{d}k}\cos(k\omega_{\mathrm{e}}t + \mu_{\mathrm{d}k}) \\ i_{\mathrm{q}} = i_{\mathrm{q0}} + \sum i_{\mathrm{q}k} = i_{\mathrm{q0}} + \sum I_{\mathrm{q}k}\sin(k\omega_{\mathrm{e}}t + \mu_{\mathrm{q}k}) \end{cases} \tag{3}$$

$$\begin{cases} \lambda_{\mathrm{d}} = \lambda_{\mathrm{d0}} + \sum \lambda_{\mathrm{d}k} = \lambda_{\mathrm{d0}} + \sum \chi_{\mathrm{d}k}\cos(k\omega_{\mathrm{e}}t + \alpha_{\mathrm{d}k}) \\ \lambda_{\mathrm{q}} = \lambda_{\mathrm{q0}} + \sum \lambda_{\mathrm{q}k} = \lambda_{\mathrm{q0}} + \sum \chi_{\mathrm{q}k}\sin(k\omega_{\mathrm{e}}t + \alpha_{\mathrm{q}k}) \end{cases} \tag{4}$$

$$\begin{cases} \Delta v_{\mathrm{d\_z}} = \Delta v_{\mathrm{d0\_}z} \\ +\Delta v_{\mathrm{d}k\_\mathrm{z}} = \Delta v_{\mathrm{d0\_}z} + \sum V_{\mathrm{d}k\_z}\cos(k\omega_{\mathrm{e}}t + \sigma_{\mathrm{d}k}) \\ \Delta v_{\mathrm{q\_z}} = \Delta v_{\mathrm{q0\_}z} \\ +\Delta v_{\mathrm{q}k\_z} = \Delta v_{\mathrm{q0\_}z} + \sum V_{\mathrm{q}k\_z}\cos(k\omega_{\mathrm{e}}t + \sigma_{\mathrm{d}k}) \end{cases} \tag{5}$$

where $v_{\mathrm{d0\_m}}$, $v_{\mathrm{q0\_m}}$, $v_{\mathrm{d}k\_\mathrm{m}}$, and $v_{\mathrm{q}k\_\mathrm{m}}$ are the dc components and the *k*th harmonic components of the *d*-axis and *q*-axis stator voltages of the IPMSM; $V_{\mathrm{d}k\_\mathrm{m}}$, $V_{\mathrm{q}k\_\mathrm{m}}$, $\phi_{\mathrm{d}k\_\mathrm{m}}$, and $\phi_{\mathrm{q}k\_\mathrm{m}}$ are the amplitude and initial phase angle of *k*th harmonics in *d*-axis and *q*-axis stator voltages; i_{d0} and i_{q0} are the dc components in the *d*-axis and *q*-axis currents; $i_{\mathrm{d}k}$ and $i_{\mathrm{q}k}$ are the *k*th harmonic components in the *d*-axis and *q*-axis currents; $I_{\mathrm{d}k}$, $I_{\mathrm{q}k}$, $\mu_{\mathrm{d}k}$, and $\mu_{\mathrm{q}k}$ are the amplitude and initial phase angle of *k*th current harmonic components in the *d*-axis and *q*-axis currents; λ_{d0}, λ_{q0}, $\lambda_{\mathrm{d}k}$, and $\lambda_{\mathrm{q}k}$ are the dc components and *k*th harmonic components of permanent magnet flux linkage; $\chi_{\mathrm{d}k}$, $\chi_{\mathrm{q}k}$, $\alpha_{\mathrm{d}k}$, and $\alpha_{\mathrm{q}k}$ are the amplitude and initial phase angle of *k*th permanent magnet flux linkage harmonic components; $\Delta v_{\mathrm{d0\_}z}$, $\Delta v_{\mathrm{q0\_}z}$, $\Delta v_{\mathrm{d}k\_z}$, and $\Delta v_{\mathrm{q}k\_z}$ are the dc components and *k*th harmonic components of the voltage harmonics induced by dead time of the inverter; $V_{\mathrm{d}k\_\mathrm{z}}$, $V_{\mathrm{q}k\_\mathrm{z}}$, $\sigma_{\mathrm{d}k}$, and $\sigma_{\mathrm{q}k}$ are the amplitude and initial phase angle of *k*th voltage harmonics induced by dead time of the inverter; $k = 6, 12, \ldots$.

For field-oriented control system, the actual three-phase current of the motor need to be converted into *d*-axis and *q*-axis

current through coordinate transformation, and then the difference between the transformed values and references is used as the input of *d*-axis and *q*-axis current controllers. Furthermore, the actual motor current will also be used in the decoupling terms of *d*-axis and *q*-axis current controllers. Because the actual motor current contains harmonics, the output voltage of *d*-axis and *q*-axis current controllers will contain a certain amount of harmonics, which is bound to have a further impact on the current harmonics. The *d*-axis and *q*-axis voltages output by the current controllers, which are composed of PI and feedforward decoupling term, can be expressed as

$$\begin{cases} v_{\mathrm{d\_c}}=k_{\mathrm{pd}}\left(i_{\mathrm{dref}}-i_{\mathrm{d}}\right) \\ +k_{\mathrm{id}}\int_0^t\left(i_{\mathrm{dref}}-i_{\mathrm{d}}\right)\mathrm{d}t-\omega_{\mathrm{e}}L_{\mathrm{q0}}i_{\mathrm{q}} \\ v_{\mathrm{q\_c}}=k_{\mathrm{pq}}\left(i_{\mathrm{qref}}-i_{\mathrm{q}}\right) \\ +k_{\mathrm{iq}}\int_0^t\left(i_{\mathrm{qref}}-i_{\mathrm{q}}\right)\mathrm{d}t+\omega_{\mathrm{e}}L_{\mathrm{d0}}i_{\mathrm{d}}+\omega_{\mathrm{e}}\lambda_{\mathrm{d0}} \end{cases} \tag{6}$$

where $v_{\mathrm{d\_c}}$ and $v_{\mathrm{q\_c}}$ are the *d*-axis and *q*-axis voltages, respectively, which current controller output; L_{d0} and L_{q0} are the nominal value of the *d*-axis and *q*-axis inductance, respectively; $k_{\mathrm{pd}}, k_{\mathrm{pq}}, k_{\mathrm{id}}$, and k_{iq} are the proportional terms and integral terms of PI; i_{dref} and i_{qref} are the *d*-axis and *q*-axis current references, respectively.

The *d*-axis and *q*-axis voltages, which current controller output, as shown in (6), can be expressed as

$$\begin{cases} v_{\mathrm{d\_c}}=v_{\mathrm{d0\_c}} \\ +\sum v_{\mathrm{d}k\_\mathrm{c}}=v_{\mathrm{d0\_c}}+\sum V_{\mathrm{d}k\_\mathrm{c}}\cos(k\omega_{\mathrm{e}}t+\phi_{\mathrm{d}k\_\mathrm{c}}) \\ v_{\mathrm{q\_c}}=v_{\mathrm{q0\_c}} \\ +\sum v_{\mathrm{q}k\_\mathrm{c}}=v_{\mathrm{q0\_c}}+\sum V_{\mathrm{q}k\_\mathrm{c}}\sin(k\omega_{\mathrm{e}}t+\phi_{\mathrm{q}k\_\mathrm{c}}) \end{cases} \tag{7}$$

where $v_{\mathrm{d0\_c}}$, $v_{\mathrm{q0\_c}}$, $v_{\mathrm{d}k\_\mathrm{c}}$, and $v_{\mathrm{q}k\_\mathrm{c}}$ are the dc components and *k*th harmonic components of the voltages, which current controller output; $V_{\mathrm{d}k\_\mathrm{c}}$, $V_{\mathrm{q}k\_\mathrm{c}}$, $\phi_{\mathrm{d}k\_\mathrm{c}}$, and $\phi_{\mathrm{q}k\_\mathrm{c}}$ are the amplitude and initial phase angle of *k*th harmonics in the voltages, which current controller output.

Digital control delay is an important reason that lead to the inconsistency between the voltages output by current controller and the actual voltages applied to IPMSM. If the voltages output by current controller are corrected as this, the voltages actually apply to IPMSM can be consistent with the voltage output by the controller in fundamental [20]

$$\begin{cases} v_{\mathrm{d\_com}}=m\left[v_{\mathrm{d\_c}}\cos(1.5\omega_{\mathrm{e}}T_{\mathrm{s}})-v_{\mathrm{q\_c}}\sin(1.5\omega_{\mathrm{e}}T_{\mathrm{s}})\right] \\ v_{\mathrm{q\_com}}=m\left[v_{\mathrm{d\_c}}\sin(1.5\omega_{\mathrm{e}}T_{\mathrm{s}})+v_{\mathrm{q\_c}}\cos(1.5\omega_{\mathrm{e}}T_{\mathrm{s}})\right] \end{cases} \tag{8}$$

$$m=\frac{\omega_{\mathrm{e}}T_{\mathrm{s}}}{2\sin(0.5\omega_{\mathrm{e}}T_{\mathrm{s}})} \tag{9}$$

where $v_{\mathrm{d\_com}}$ and $v_{\mathrm{q\_com}}$ are the *d*–*q* axis voltages, which current controller output, after modified; T_{s} is the control period.

B. Proposed Calculation Model of DQ*-Axis Current Harmonics in FOC System*

Through research, we find that the phase angles are still different between the voltage harmonics output by the *d*-axis and *q*-axis current controllers and the voltage harmonics actually apply to the IPMSM after aforementioned correction. Taking *d*-axis voltage as an example, Fig. 1 is a timing diagram of current sampling, voltage output of *d*-axis current controller,

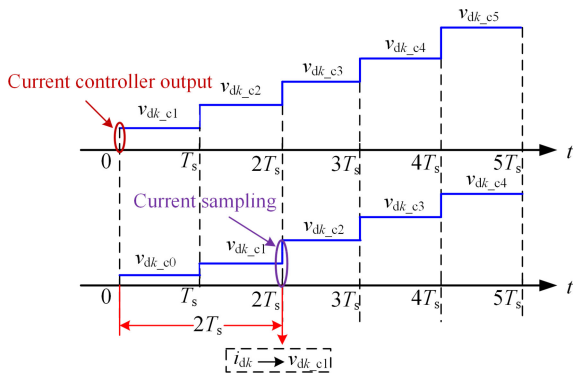

Fig. 1. Time sequence of current sampling, voltage calculation, and voltage output.

and voltage apply to the IPMSM. It can be seen from the figure that when the sampled current is taken as the actual current of the motor control system, it can be considered that the *d*-axis voltage actually applies to the IPMSM lags behind the voltage output by the *d*-axis current controller by two control periods. The relationship between the *k*th voltage harmonic output by the *d*-axis current controller and the *k*th voltage harmonic actually apply to IPMSM is as follows:

$$\begin{aligned} &V_{\mathrm{d}k\_\mathrm{c}}\cos(k\omega_{\mathrm{e}}\left(t-2T_{\mathrm{s}}\right)+\phi_{\mathrm{d}k\_\mathrm{c}}) \\ &=V_{\mathrm{d}k\_\mathrm{m}}\cos(k\omega_{\mathrm{e}}t+\phi_{\mathrm{d}k\_m}). \end{aligned} \tag{10}$$

Similarly, the relationship between the *k*th voltage harmonic output by the *q*-axis current controller and the *k*th voltage harmonic actually apply to IPMSM is as follows:

$$V_{\mathrm{q}k\_\mathrm{c}}\sin(k\omega_{\mathrm{e}}\left(t-2T_{\mathrm{s}}\right)+\phi_{\mathrm{q}k\_\mathrm{c}})=V_{\mathrm{q}k\_\mathrm{m}}\sin(k\omega_{\mathrm{e}}t+\phi_{\mathrm{q}k\_m}). \tag{11}$$

Based on the aforementioned analysis and Section II-A, the current loop structure block diagram of IPMSM field-oriented control system at the level of *k*th harmonic can be obtained, as shown in Fig. 2. Taking the sixth harmonic as an example, the proposed calculation model of *d*-axis and *q*-axis current harmonics is described as follows. Based on the aforementioned analysis and Fig. 2, the voltage harmonics in the *d*-axis and *q*-axis current loop of the FOC system should be composed of three parts: voltage harmonics induced by inverter dead time, voltage harmonics induced by permanent magnet flux linkage, and voltage harmonics induced by feedforward decoupling incomplete.

Sixth voltage harmonics induced by the sixth permanent magnet flux harmonic are expressed as

$$\begin{bmatrix}\Delta v_{\mathrm{d6\_}\lambda}\\ \Delta v_{\mathrm{q6\_}\lambda}\end{bmatrix}=\begin{bmatrix}\frac{\mathrm{d}\lambda_{\mathrm{d6}}}{\mathrm{d}t}-\omega_{\mathrm{e}}\lambda_{\mathrm{q6}}\\ \frac{\mathrm{d}\lambda_{\mathrm{q6}}}{\mathrm{d}t}+\omega_{\mathrm{e}}\lambda_{\mathrm{d6}}\end{bmatrix}=\begin{bmatrix}V_{\mathrm{d6\_}\lambda}\cos(6\omega_{\mathrm{e}}t+\delta_{\mathrm{d6}})\\ V_{\mathrm{q6\_}\lambda}\sin(6\omega_{\mathrm{e}}t+\delta_{\mathrm{q6}})\end{bmatrix} \tag{12}$$

where $V_{\mathrm{d}k\_\lambda}$, $V_{\mathrm{q}k\_\lambda}$, δ_{d6}, and δ_{q6} are the amplitude and initial phase angle of sixth voltage harmonics induced by permanent magnet flux linkage harmonics

$$\begin{bmatrix}\delta_{\mathrm{d6}}\\ \delta_{\mathrm{q6}}\end{bmatrix}=\begin{bmatrix}\arctan(\frac{\chi_{\mathrm{q6}}\sin\alpha_{\mathrm{q6}}+6\chi_{\mathrm{d6}}\sin\alpha_{\mathrm{d6}}}{\chi_{\mathrm{q6}}\cos\alpha_{\mathrm{q6}}+6\chi_{\mathrm{d6}}\cos\alpha_{\mathrm{d6}}})\\ \arctan(\frac{\chi_{\mathrm{d6}}\sin\alpha_{\mathrm{d6}}+6\chi_{\mathrm{q6}}\sin\alpha_{\mathrm{q6}}}{\chi_{\mathrm{d6}}\cos\alpha_{\mathrm{d6}}+6\chi_{\mathrm{q6}}\cos\alpha_{\mathrm{q6}}})\end{bmatrix}.$$

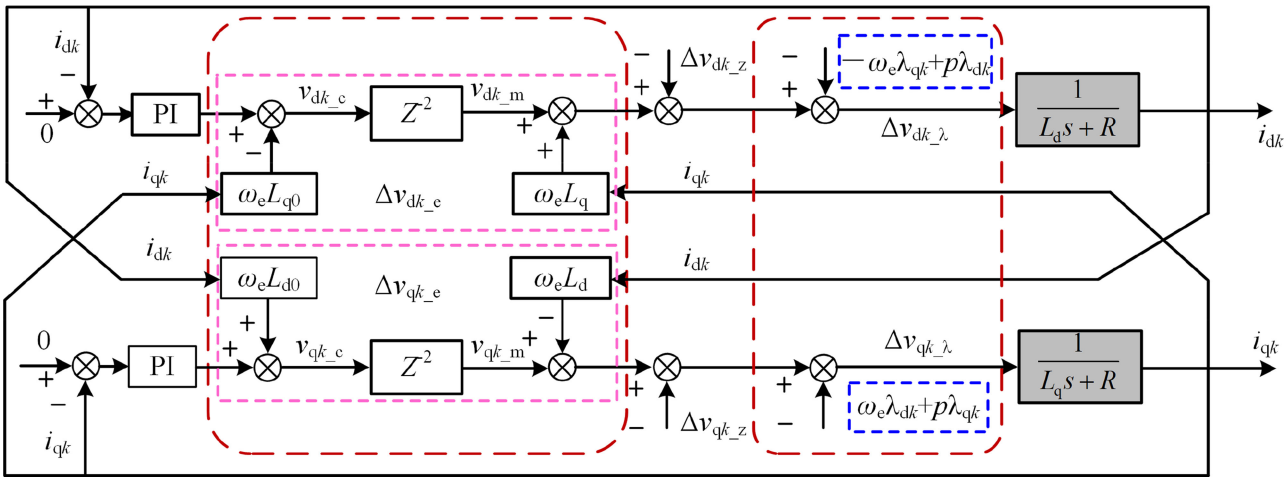

Fig. 2. Current loop structure block diagram of IPMSM field-oriented control system.

Due to the variation of motor parameters in the actual motor control, the inductance in the feedforward decoupling term will be different from the actual inductance of the motor. And the phase error between the feedforward decoupling term and the actual coupling term in the motor caused by digital control delay will further aggravate the incomplete decoupling. The sixth voltage harmonics induced by this can be expressed as

Δv_{d6_e} and Δv_{q6_e} can also be expressed as

$$\begin{bmatrix}\Delta v_{d6\_e}\\ \Delta v_{q6\_e}\end{bmatrix}=\begin{bmatrix}V_{d6\_e}\cos(6\omega_e t+\beta_{d6})\\ V_{q6\_e}\sin(6\omega_e t+\beta_{q6})\end{bmatrix} \tag{14}$$

where V_{d6_e}, V_{q6_e}, β_{d6}, and β_{q6} are the amplitude and initial phase angle of sixth voltage harmonics caused by decoupling incompletely

$$\phi_{TD}=12T_s\omega_e$$

$$\begin{bmatrix}V_{d6\_e}\\ V_{q6\_e}\end{bmatrix}=\begin{bmatrix}\omega_e I_{q6}\sqrt{{L_q}^2+{L_{q0}}^2-2L_qL_{q0}\cos\phi_{TD}}\\ \omega_e I_{d6}\sqrt{{L_d}^2+{L_{d0}}^2-2L_dL_{d0}\cos\phi_{TD}}\end{bmatrix}$$

$$\begin{bmatrix}\beta_{d6}\\ \beta_{q6}\end{bmatrix}=\begin{bmatrix}\mu_{q6}+\arctan(\frac{L_{q0}\cos\phi_{TD}-L_q}{L_{q0}\sin\phi_{TD}})\\ -\mu_{d6}+\arctan(\frac{L_{d0}\cos\phi_{TD}-L_d}{L_{d0}\sin\phi_{TD}})\end{bmatrix}.$$

Combing together the voltage harmonics induced by dead time of inverter, permanent magnet flux harmonics, and incomplete feedforward decoupling, the total sixth voltage harmonics in IPMSM field-oriented control system can be expressed as

$$\begin{cases}\Delta v_{d6}=\Delta v_{d6\_z}+\Delta v_{d6\_\lambda}+\Delta v_{d6\_e}=V_{d6}\cos(6\omega_e t+\gamma_{d6})\\ \Delta v_{q6}=\Delta v_{q6\_z}+\Delta v_{q6\_\lambda}+\Delta v_{q6\_e}=V_{q6}\sin(6\omega_e t+\gamma_{q6})\end{cases} \tag{15}$$

where V_{d6}, V_{q6}, γ_{d6}, and γ_{q6} are the amplitude and initial phase angle of total sixth voltage harmonics.

Based on (1), (6), (10), (11), and (15), the relationship between the sixth voltage harmonics and current harmonics in IPMSM field-oriented control system can be obtained as

$$\begin{cases}\Delta v_{d6}=Ri_{d6}(\theta_{id})\\ \quad+L_d\frac{di_{d6}(\theta_{id})}{dt}+k_{pd}i_{d6}(\theta_{id}-\phi_{TD})+k_{id}\int_0^t i_{d6}(\theta_{id}-\phi_{TD})dt\\ \Delta v_{q6}=Ri_{q6}(\theta_{iq})\\ \quad+L_q\frac{di_{q}(\theta_{iq})}{dt}+k_{pq}i_{q6}(\theta_{iq}-\phi_{TD})+k_{iq}\int_0^t i_{q6}(\theta_{id}-\phi_{TD})dt\end{cases} \tag{16}$$

$$\begin{cases}\theta_{id}=6\omega_e t+\mu_{d6}\\ \theta_{iq}=6\omega_e t+\mu_{q6}\end{cases}. \tag{17}$$

Furthermore, the calculation model of the d-axis and q-axis sixth current harmonics can be obtained, as shown in (18). It can be seen from it that the amplitudes of d-axis and q-axis sixth current harmonics are affected by the sixth voltage harmonic amplitude, PI parameters, inductance parameters, and the speed of IPMSM.

The traditional calculation model ignores the influence of voltage harmonics generated by d-axis and q-axis current controllers and digital control delay, and obtains the following

$$\begin{bmatrix}V_{d6\_\lambda}\\ V_{q6\_\lambda}\end{bmatrix}=\begin{bmatrix}\omega_e\sqrt{(\chi_{q6}\sin\alpha_{q6}+6\chi_{d6}\sin\alpha_{d6})^2+(\chi_{q6}\cos\alpha_{q6}+6\chi_{d6}\cos\alpha_{d6})^2}\\ \omega_e\sqrt{(\chi_{d6}\sin\alpha_{d6}+6\chi_{q6}\sin\alpha_{q6})^2+(\chi_{d6}\cos\alpha_{d6}+6\chi_{q6}\cos\alpha_{q6})^2}\end{bmatrix}$$

$$\begin{bmatrix}\Delta v_{d6\_e}\\ \Delta v_{q6\_e}\end{bmatrix}=\begin{bmatrix}\omega_e L_{q0}I_{q6}\sin(6\omega_e(t-2T_s)+\mu_{q6})-\omega_e L_q I_{q6}\sin(6\omega_e t+\mu_{q6})\\ \omega_e L_{d0}I_{d6}\cos(6\omega_e(t-2T_s)+\mu_{d6})-\omega_e L_d I_{d6}\cos(6\omega_e t+\mu_{d6})\end{bmatrix}. \tag{13}$$

simplified calculation formulas [3]–[7]:

$$\begin{cases} i_{\mathrm{d}6} = \frac{\Delta v_{\mathrm{d}6\_z}+\Delta v_{\mathrm{d}6\_\lambda}}{\sqrt{R^2+(6\omega_{\mathrm{e}}L_{\mathrm{d}})^2}} \\ i_{\mathrm{q}6} = \frac{\Delta v_{\mathrm{q}6\_z}+\Delta v_{\mathrm{q}6\_\lambda}}{\sqrt{R^2+(6\omega_{\mathrm{e}}L_{\mathrm{q}})^2}} \end{cases}. \tag{19}$$

Compared with (18) and (19), it can be seen that the current harmonic calculation model deduced by this article can comprehensively reflect the influencing factors of d-axis and q-axis current harmonics in IPMSM field-oriented control system.

III. Improved Current Harmonic Control Strategy

The proposed current harmonic control strategy consists of two parts: current harmonic extraction method and designing current harmonic regulator. The proposed method is described and analyzed as follows.

A. Accurate Extraction Method of D*-Axis,* Q*-Axis Current Harmonic Characteristic Quantities Based on MSRFT*

In order to achieve good performance of current harmonic control, the accuracy of current harmonic extraction is important. The sampled phase currents can be expressed as

$$\begin{bmatrix} i_{\mathrm{a}} \\ i_{\mathrm{b}} \\ i_{\mathrm{c}} \end{bmatrix} = \begin{bmatrix} \sum I_{\mathrm{s}f}\cos(f\omega_{\mathrm{e}}t+\eta_f) \\ \sum I_{\mathrm{s}f}\cos(f(\omega_{\mathrm{e}}t-\frac{2}{3}\pi)+\eta_f) \\ \sum I_{\mathrm{s}f}\cos(f(\omega_{\mathrm{e}}t+\frac{2}{3}\pi)+\eta_f) \end{bmatrix} \tag{20}$$

where $I_{\mathrm{s}f}$ and η_f are the amplitude and initial phase angle of phase current harmonics; $f = 1, 5, 7, 11, 13\ldots$.

Then, the sampled phase currents are passed through fifth synchronous rotating frame transformation

$$\begin{cases} i_{\mathrm{dh}}^{5\mathrm{dq}} = I_{\mathrm{s}5}\cos\eta_5 \\ +I_{\mathrm{s}1}\cos(6\omega_{\mathrm{e}}t+\eta_1)+I_{\mathrm{s}7}\cos(12\omega_{\mathrm{e}}t+\eta_7) \\ +I_{\mathrm{s}11}\cos(6\omega_{\mathrm{e}}t+\eta_{11})+I_{\mathrm{s}13}\cos(18\omega_{\mathrm{e}}t+\eta_{13})+\cdots \\ i_{\mathrm{qh}}^{5\mathrm{dq}} = I_{\mathrm{s}5}\sin\eta_5 - I_{\mathrm{s}1}\sin(6\omega_{\mathrm{e}}t+\eta_1) - I_{\mathrm{s}7}\sin(12\omega_{\mathrm{e}}t+\eta_7) \\ +I_{\mathrm{s}11}\sin(6\omega_{\mathrm{e}}t+\eta_{11}) - I_{\mathrm{s}13}\sin(18\omega_{\mathrm{e}}t+\eta_{13})+\cdots \end{cases}. \tag{21}$$

Similarly, the sampled phase currents are passed through seventh synchronous rotating frame transformation

$$\begin{cases} i_{\mathrm{dh}}^{7\mathrm{dq}} = I_{\mathrm{s}7}\cos\eta_7 \\ -I_{\mathrm{s}1}\cos(6\omega_{\mathrm{e}}t-\eta_1)+I_{\mathrm{s}5}\cos(12\omega_{\mathrm{e}}t+\eta_5) \\ +I_{\mathrm{s}11}\cos(18\omega_{\mathrm{e}}t+\eta_{11})+I_{\mathrm{s}13}\cos(6\omega_{\mathrm{e}}t+\eta_{13})+\cdots \\ i_{\mathrm{qh}}^{7\mathrm{dq}} = I_{\mathrm{s}7}\sin\eta_7 - I_{\mathrm{s}1}\sin(6\omega_{\mathrm{e}}t-\eta_1) - I_{\mathrm{s}5}\sin(12\omega_{\mathrm{e}}t+\eta_5) \\ -I_{\mathrm{s}11}\sin(18\omega_{\mathrm{e}}t+\eta_{11})+I_{\mathrm{s}13}\sin(6\omega_{\mathrm{e}}t+\eta_{13})+\cdots \end{cases}. \tag{22}$$

FLPF can realize the separation of dc and ac. Equations (21) and (22) are, respectively, passed through FLPF to obtain the characteristic quantities ($I_{\mathrm{s}7}\cos\eta_7$,$I_{\mathrm{s}7}\sin\eta_7$,$I_{\mathrm{s}5}\cos\eta_5$, and $I_{\mathrm{s}5}\sin\eta_5$) of the fifth and seventh harmonics in the three-phase currents. The traditional current harmonic extraction block diagram is shown in Fig. 3.

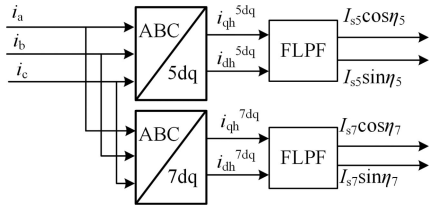

Fig. 3. Block diagram of traditional method of current harmonic extraction.

However, for the motor control system with high current, the fundamental component in the phase current is far greater than the harmonic component. And the attenuation of the actual FLPF to the signal at the cutoff frequency will not be zero, which makes it difficult to completely eliminate the ac quantities corresponding to the fundamental current in the phase currents and affect the extraction of harmonic characteristic quantities. This is the reason why the current harmonic extraction method based on MSRFT is difficult to be effectively applied to motor control system. In order to improve the application performance of current harmonic extraction method based on MSRFT in motor control system, an improved current harmonic extraction method is proposed in this article. This method aims to extract the sixth d-axis and q-axis harmonic characteristic quantities, which is based on the accurate extraction of the fifth and seventh harmonic characteristic quantities of phase currents.

It can be seen from the aforementioned analysis that the fundamental component of phase currents is the main factor affecting the accuracy of current harmonic characteristic quantities extraction. In order to ensure that the extracted information is not affected by them, this article first subtracts the fundamental current from phase currents, which are sampled. The fundamental current can be reconstructed from the d-axis and q-axis current references, as shown in (23)

$$\begin{bmatrix} i_{\mathrm{a\_fun}} \\ i_{\mathrm{b\_fun}} \\ i_{\mathrm{c\_fun}} \end{bmatrix} = \sqrt{i_{\mathrm{dref}}^2+i_{\mathrm{qref}}^2} \begin{bmatrix} \cos(\theta_{\mathrm{e}}+\frac{\pi}{2}+\arccos(\frac{i_{\mathrm{qref}}}{\sqrt{i_{\mathrm{dref}}^2+i_{\mathrm{qref}}^2}})) \\ \cos(\theta_{\mathrm{e}}-\frac{2}{3}\pi+\frac{\pi}{2}+\arccos(\frac{i_{\mathrm{qref}}}{\sqrt{i_{\mathrm{dref}}^2+i_{\mathrm{qref}}^2}})) \\ \cos(\theta_{\mathrm{e}}+\frac{2}{3}\pi+\frac{\pi}{2}+\arccos(\frac{i_{\mathrm{qref}}}{\sqrt{i_{\mathrm{dref}}^2+i_{\mathrm{qref}}^2}})) \end{bmatrix} \tag{23}$$

where $i_{\mathrm{a\_fun}}$, $i_{\mathrm{b\_fun}}$, and $i_{\mathrm{c\_fun}}$ are the fundamental component of the reconstructed three-phase currents; $i_{\mathrm{d\_ref}}$ and $i_{\mathrm{q\_ref}}$ are the d-axis and q-axis current references, respectively; θ_{e} is the position angle.

$$\begin{aligned} i_{\mathrm{d}6} &= \frac{V_{\mathrm{d}6}}{\sqrt{(R+k_{\mathrm{pd}}\cos\phi_{\mathrm{TD}}-\frac{k_{\mathrm{id}}}{6\omega_{\mathrm{e}}}\sin\phi_{\mathrm{TD}})^2+(6\omega_{\mathrm{e}}L_{\mathrm{d}}-k_{\mathrm{pd}}\sin\phi_{\mathrm{TD}}-\frac{k_{\mathrm{id}}}{6\omega_{\mathrm{e}}}\cos\phi_{\mathrm{TD}})^2}}\cos(6\omega_{\mathrm{e}}t+\mu_{\mathrm{d}6}) \\ i_{\mathrm{q}6} &= \frac{V_{\mathrm{q}6}}{\sqrt{(R+k_{\mathrm{pq}}\cos\phi_{\mathrm{TD}}-\frac{k_{\mathrm{iq}}}{6\omega_{\mathrm{e}}}\sin\phi_{\mathrm{TD}})^2+(6\omega_{\mathrm{e}}L_{\mathrm{q}}-k_{\mathrm{pq}}\sin\phi_{\mathrm{TD}}-\frac{k_{\mathrm{iq}}}{6\omega_{\mathrm{e}}}\cos\phi_{\mathrm{TD}})^2}}\sin(6\omega_{\mathrm{e}}t+\mu_{\mathrm{q}6}) \end{aligned} \tag{18}$$

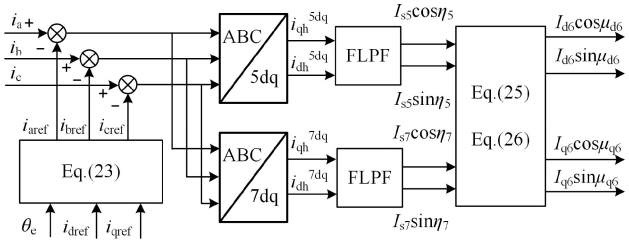

Fig. 4. Block diagram of proposed d-axis and q-axis current harmonic characteristic quantities extraction method.

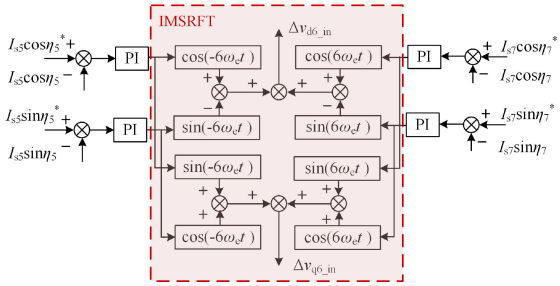

Fig. 5. Block diagram of traditional PI current harmonic regulator.

Then, passing it through fifth synchronous rotating frame transformation and FLPF, the fifth harmonic characteristic quantities in the phase current can be obtained. The seventh harmonic characteristic quantities can also be obtained as this.

Furthermore, after the 3/2 coordinate transformation of (20), the fifth and seventh current harmonics in the phase currents are shifted into the form of sixth current harmonics in the d–q axis frame, and the specific relationship can be expressed as

$$\begin{bmatrix} i_{\mathrm{d6}} \\ i_{\mathrm{q6}} \end{bmatrix} = \begin{bmatrix} I_{\mathrm{s7}}\cos(6\omega_{\mathrm{e}}t+\eta_7) + I_{\mathrm{s5}}\cos(6\omega_{\mathrm{e}}t+\eta_5) \\ I_{\mathrm{s7}}\sin(6\omega_{\mathrm{e}}t+\eta_7) - I_{\mathrm{s5}}\sin(6\omega_{\mathrm{e}}t+\eta_5) \end{bmatrix} \tag{24}$$

$$\begin{cases} I_{\mathrm{d6}}\cos\mu_{\mathrm{d6}} = I_{\mathrm{s7}}\cos\eta_7 + I_{\mathrm{s5}}\cos\eta_5 \\ I_{\mathrm{d6}}\sin\mu_{\mathrm{d6}} = I_{\mathrm{s7}}\sin\eta_7 + I_{\mathrm{s5}}\sin\eta_5 \end{cases} \tag{25}$$

$$\begin{cases} I_{\mathrm{q6}}\cos\mu_{\mathrm{q6}} = I_{\mathrm{s7}}\cos\eta_7 - I_{\mathrm{s5}}\cos\eta_5 \\ I_{\mathrm{q6}}\sin\mu_{\mathrm{q6}} = I_{\mathrm{s7}}\sin\eta_7 - I_{\mathrm{s5}}\sin\eta_5 \end{cases}. \tag{26}$$

Equations (25) and (26) describe the relationship between the sixth harmonic current characteristic quantities in d-axis, q-axis currents and the fifth, seventh harmonic current characteristic quantities in phase currents. Combined with the extracted characteristic quantities of the fifth and seventh harmonic currents, the sixth harmonic characteristic quantities in d-axis and q-axis currents can be obtained. The block diagram of the proposed current harmonic characteristic quantities extraction is shown in Fig. 4.

B. Design of PI Current Harmonic Regulator Based on Unified Coordinate Frame

The current harmonic regulator is the key to realize that the motor harmonic current follows the reference. The traditional PI current harmonic regulator generally generates the desired sixth voltage harmonic characteristic quantities by passing fifth and seventh current harmonic characteristic quantities extracted through four PIs, respectively, and then injects them into the control system through IMSRFT. Its structure is shown in Fig. 5. The traditional current harmonic regulator mainly has these problems shown as follow.

1) The fifth and seventh current harmonic characteristic quantities are the quantities in three-phase coordinate frame. And sixth voltage harmonic characteristic quantities are the quantities in d–q coordinate frame. In order to control the fifth and seventh current harmonic characteristic quantities in the d–q coordinate frame, it is necessary to know the relationship between the fifth, seventh current harmonic characteristic quantities and the sixth voltage harmonic characteristic quantities. However, the mathematical relationship between the variables in different coordinate frame is difficult to analyze.
2) Because the d-axis and q-axis current controllers are established in the d–q coordinate system, it is difficult to consider the influence of the sixth voltage harmonic output by the d-axis and q-axis current controllers on the fifth and seventh current harmonics in phase current.
3) The existing methods do not consider the influence of digital control delay on the initial phase angle of injected harmonic voltage.

Equation (16) in Section II-B, which the influence of current controller and digital control delay takes fully into account, describes the relationship between the sixth voltage harmonics and the sixth current harmonics of IPMSM FOC system in d–q coordinate frame. Furthermore, (16) can be expressed as follows, as shown in (27). The differential term and integral term in it can be write as

$$\begin{cases} \frac{\mathrm{d}I_{\mathrm{d6}}\cos(6\omega_{\mathrm{e}}t+\mu_{\mathrm{d6}})}{\mathrm{d}t} = -6\omega_{\mathrm{e}}I_{\mathrm{d6}}\sin(6\omega_{\mathrm{e}}t+\mu_{\mathrm{d6}}) \\ \frac{\mathrm{d}I_{\mathrm{q6}}\sin(6\omega_{\mathrm{e}}t+\mu_{\mathrm{q6}})}{\mathrm{d}t} = 6\omega_{\mathrm{e}}I_{\mathrm{q6}}\cos(6\omega_{\mathrm{e}}t+\mu_{\mathrm{q6}}) \end{cases} \tag{28}$$

$$\begin{cases} \int_0^t I_{\mathrm{d6}}\cos(6\omega_{\mathrm{e}}t+\mu_{\mathrm{d6}}-\phi_{\mathrm{TD}}) \\ = \frac{I_{\mathrm{d6}}}{6\omega_{\mathrm{e}}}\sin(6\omega_{\mathrm{e}}t+\mu_{\mathrm{d6}}-\phi_{\mathrm{TD}}) - \frac{I_{\mathrm{d6}}}{6\omega_{\mathrm{e}}}\sin(\mu_{\mathrm{d6}}-\phi_{\mathrm{TD}}) \\ \int_0^t I_{\mathrm{q6}}\sin(6\omega_{\mathrm{e}}t+\mu_{\mathrm{q6}}-\phi_{\mathrm{TD}}) \\ = -\frac{I_{\mathrm{q6}}}{6\omega_{\mathrm{e}}}\cos(6\omega_{\mathrm{e}}t+\mu_{\mathrm{q6}}-\phi_{\mathrm{TD}}) + \frac{I_{\mathrm{q6}}}{6\omega_{\mathrm{e}}}\cos(\mu_{\mathrm{q6}}-\phi_{\mathrm{TD}}) \end{cases}. \tag{29}$$

$$\begin{cases} V_{\mathrm{d6}}\cos(6\omega_{\mathrm{e}}t+\gamma_{\mathrm{d6}}) = RI_{\mathrm{d6}}\cos(6\omega_{\mathrm{e}}t+\mu_{\mathrm{d6}}) \\ +L_{\mathrm{d}}\frac{\mathrm{d}I_{\mathrm{d6}}\cos(6\omega_{\mathrm{e}}t+\mu_{\mathrm{d6}})}{\mathrm{d}t} + k_{\mathrm{pd}}I_{\mathrm{d6}}\cos(6\omega_{\mathrm{e}}t+\mu_{\mathrm{d6}}-\phi_{\mathrm{TD}}) + k_{\mathrm{id}}\int_0^t I_{\mathrm{d6}}\cos(6\omega_{\mathrm{e}}t+\mu_{\mathrm{d6}}-\phi_{\mathrm{TD}})\mathrm{d}t \\ V_{\mathrm{q6}}\sin(6\omega_{\mathrm{e}}t+\gamma_{\mathrm{q6}}) = RI_{\mathrm{q6}}\sin(6\omega_{\mathrm{e}}t+\mu_{\mathrm{q6}}) \\ +L_{\mathrm{q}}\frac{\mathrm{d}I_{\mathrm{q6}}\sin(6\omega_{\mathrm{e}}t+\mu_{\mathrm{q6}})}{\mathrm{d}t} + k_{\mathrm{pq}}I_{\mathrm{q6}}\sin(6\omega_{\mathrm{e}}t+\mu_{\mathrm{q6}}-\phi_{\mathrm{TD}}) + k_{\mathrm{iq}}\int_0^t I_{\mathrm{q6}}\sin(6\omega_{\mathrm{e}}t+\mu_{\mathrm{q6}}-\phi_{\mathrm{TD}})\mathrm{d}t \end{cases} \tag{27}$$

Take the ac quantity in (29), and then combine (27) and (28) to obtain

$$\begin{cases} V_{\mathrm{d6}}\cos\gamma_{\mathrm{d6}}=\frac{\cos\Delta\varepsilon_{\mathrm{d}}}{\tau_{\mathrm{d}}}I_{\mathrm{d6}}\cos\mu_{\mathrm{d6}}+\frac{sin\Delta\varepsilon_{\mathrm{d}}}{\tau_{\mathrm{d}}}I_{\mathrm{d6}}\sin\mu_{\mathrm{d6}} \\ V_{\mathrm{d6}}\sin\gamma_{\mathrm{d6}}=\frac{\cos\Delta\varepsilon_{\mathrm{d}}}{\tau_{\mathrm{d}}}I_{\mathrm{d6}}\sin\mu_{\mathrm{d6}}-\frac{sin\Delta\varepsilon_{\mathrm{d}}}{\tau_{\mathrm{d}}}I_{\mathrm{d6}}\cos\mu_{\mathrm{d6}} \end{cases} \tag{30}$$

$$\begin{cases} V_{\mathrm{q6}}\cos\gamma_{\mathrm{q6}}=\frac{\cos\Delta\varepsilon_{\mathrm{q}}}{\tau_{\mathrm{q}}}I_{\mathrm{q6}}\cos\mu_{\mathrm{q6}}+\frac{sin\Delta\varepsilon_{\mathrm{q}}}{\tau_{\mathrm{q}}}I_{\mathrm{q6}}\sin\mu_{\mathrm{q6}} \\ V_{\mathrm{q6}}\sin\gamma_{\mathrm{q6}}=\frac{\cos\Delta\varepsilon_{\mathrm{q}}}{\tau_{\mathrm{q}}}I_{\mathrm{q6}}\sin\mu_{\mathrm{q6}}-\frac{sin\Delta\varepsilon_{\mathrm{q}}}{\tau_{\mathrm{q}}}I_{\mathrm{q6}}\cos\mu_{\mathrm{q6}} \end{cases}. \tag{31}$$

Among them

$$\begin{cases} \frac{\cos\Delta\varepsilon_{\mathrm{d}}}{\tau_{\mathrm{d}}}=R+k_{\mathrm{pd}}\cos\phi_{\mathrm{TD}}-\frac{k_{\mathrm{id}}}{6\omega_{\mathrm{e}}}\sin\phi_{\mathrm{TD}} \\ \frac{sin\Delta\varepsilon_{\mathrm{d}}}{\tau_{\mathrm{d}}}=k_{\mathrm{pd}}\sin\phi_{\mathrm{TD}}-6\omega_{\mathrm{e}}L_{\mathrm{d}}+\frac{k_{\mathrm{id}}}{6\omega_{\mathrm{e}}}\cos\phi_{\mathrm{TD}} \end{cases} \tag{32}$$

$$\begin{cases} \frac{\cos\Delta\varepsilon_{\mathrm{q}}}{\tau_{\mathrm{q}}}=R+k_{\mathrm{pq}}\cos\phi_{\mathrm{TD}}-\frac{k_{\mathrm{iq}}}{6\omega_{\mathrm{e}}}\sin\phi_{\mathrm{TD}} \\ \frac{sin\Delta\varepsilon_{\mathrm{q}}}{\tau_{\mathrm{q}}}=k_{\mathrm{pq}}\sin\phi_{\mathrm{TD}}-6\omega_{\mathrm{e}}L_{\mathrm{q}}+\frac{k_{\mathrm{iq}}}{6\omega_{\mathrm{e}}}\cos\phi_{\mathrm{TD}} \end{cases} \tag{33}$$

where τ_{d} and τ_{q} are the ratio of the sixth current harmonics amplitude to the sixth voltage harmonics amplitude; $\Delta\varepsilon_{\mathrm{d}}$ and $\Delta\varepsilon_{\mathrm{q}}$ are the difference between the phase angle of sixth voltage harmonics and the phase angle of sixth current harmonics.

Different from the traditional method of controlling the fifth and seventh current harmonic characteristic quantities in three-phase coordinate frame, this article controls the sixth current harmonic characteristic quantities in *d–q* coordinate frame. The extracted $I_{\mathrm{d6}}\cos\mu_{\mathrm{d6}}$, $I_{\mathrm{d6}}\sin\mu_{\mathrm{d6}}$, $I_{\mathrm{q6}}\cos\mu_{\mathrm{q6}}$, and $I_{\mathrm{q6}}\sin\mu_{\mathrm{q6}}$ are passed through the PI regulator to generate the desired voltage harmonics. From (30) and (31), we can clearly see the coupling relationship between the sixth *d*-axis and *q*-axis current harmonic characteristic quantities. Based on the established mathematical model, the decoupling can be easily realized. Moreover, the digital control delay will also affect the initial phase angle of the injected voltage harmonic, as follows:

$$\begin{cases} V_{\mathrm{d6}}\cos\gamma_{\mathrm{d6}}=V_{\mathrm{d6}}\cos\left(\gamma_{\mathrm{d6}}{}^{\mathrm{IN}}-\phi_{\mathrm{TD}}\right) \\ V_{\mathrm{d6}}\sin\gamma_{\mathrm{d6}}=V_{\mathrm{d6}}\sin\left(\gamma_{\mathrm{d6}}{}^{\mathrm{IN}}-\phi_{\mathrm{TD}}\right) \end{cases} \tag{34}$$

$$\begin{cases} V_{\mathrm{q6}}\cos\gamma_{\mathrm{q6}}=V_{\mathrm{q6}}\cos\left(\gamma_{\mathrm{q6}}{}^{\mathrm{IN}}-\phi_{\mathrm{TD}}\right) \\ V_{\mathrm{q6}}\sin\gamma_{\mathrm{q6}}=V_{\mathrm{q6}}\sin\left(\gamma_{\mathrm{q6}}{}^{\mathrm{IN}}+\phi_{\mathrm{TD}}\right) \end{cases}. \tag{35}$$

In order to avoid this effect, it is necessary to compensate the initial phase angle of voltage harmonics generated by current harmonic regulators

$$\begin{cases} V_{\mathrm{d6}}\cos\gamma_{\mathrm{d6}}{}^{\mathrm{IN}} \\ =V_{\mathrm{d6}}\cos\gamma_{\mathrm{d6}}{}^{*}\cos(\phi_{\mathrm{TD}})-V_{\mathrm{d6}}\sin\gamma_{\mathrm{d6}}{}^{*}\sin(\phi_{\mathrm{TD}}) \\ V_{\mathrm{d6}}\sin\gamma_{\mathrm{d6}}{}^{\mathrm{IN}} \\ =V_{\mathrm{d6}}\sin\gamma_{\mathrm{d6}}{}^{*}cos(\phi_{\mathrm{TD}})+V_{\mathrm{d6}}\cos\gamma_{\mathrm{d6}}{}^{*}\sin(\phi_{\mathrm{TD}}) \end{cases} \tag{36}$$

$$\begin{cases} V_{\mathrm{q6}}\cos\gamma_{\mathrm{q6}}{}^{\mathrm{IN}} \\ =V_{\mathrm{q6}}\cos\gamma_{\mathrm{q6}}{}^{*}\cos(\phi_{\mathrm{TD}})-V_{\mathrm{q6}}\sin\gamma_{\mathrm{q6}}{}^{*}\sin(\phi_{\mathrm{TD}}) \\ V_{\mathrm{q6}}\sin\gamma_{\mathrm{q6}}{}^{\mathrm{IN}} \\ =V_{\mathrm{q6}}\sin\gamma_{\mathrm{q6}}{}^{*}cos(\phi_{\mathrm{TD}})+V_{\mathrm{q6}}\cos\gamma_{\mathrm{q6}}{}^{*}\sin(\phi_{\mathrm{TD}}) \end{cases}. \tag{37}$$

The final injected sixth voltage harmonics can be expressed as

$$\begin{cases} \Delta v_{\mathrm{d6\_in}}=V_{\mathrm{d6}}\cos\gamma_{\mathrm{d6}}{}^{\mathrm{IN}}\cos(6\omega_{\mathrm{e}}t)-V_{\mathrm{d6}}\sin\gamma_{\mathrm{d6}}{}^{\mathrm{IN}}\sin(6\omega_{\mathrm{e}}t) \\ \Delta v_{\mathrm{q6\_in}}=V_{\mathrm{q6}}\cos\gamma_{\mathrm{q6}}{}^{\mathrm{IN}}\sin(6\omega_{\mathrm{e}}t)+V_{\mathrm{q6}}\sin\gamma_{\mathrm{q6}}{}^{\mathrm{IN}}cos(6\omega_{\mathrm{e}}t) \end{cases}. \tag{38}$$

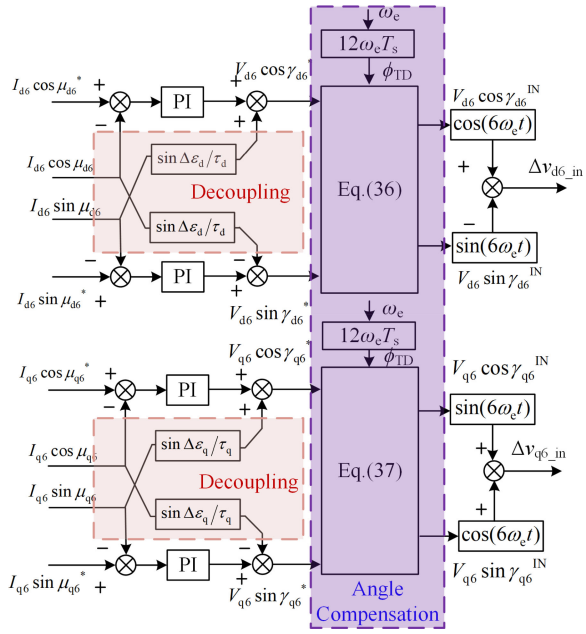

Fig. 6. Structure diagram of proposed PI current harmonic regulators based on unified coordinate frame.

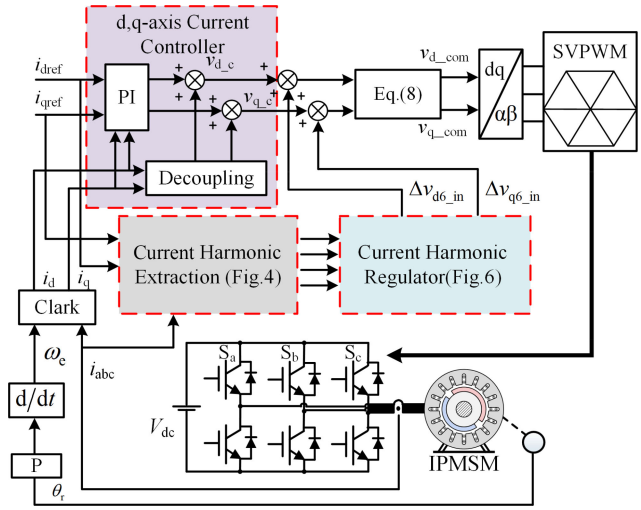

Fig. 7. Block diagram of the whole proposed control scheme.

The proposed PI current harmonic regulator based on unified coordinate frame includes two parts: current harmonic decoupling and voltage harmonic initial phase angle compensation. The specific structure block diagram is shown in Fig. 6. The total current harmonic control block diagram is shown in Fig. 7.

C. PI Parameter Design Principle and Analysis of Proposed Current Harmonic Regulators

As an example, the PI parameter design principle of the current harmonic regulators is analyzed with the *d*-axis current harmonic characteristic quantity ($I_{\mathrm{d6}}\cos\mu_{\mathrm{d6}}$). According to the mathematical relationship between *d*-axis voltage harmonics and *d*-axis current harmonics of IPMSM FOC system and the proposed current harmonic regulator, Fig. 8(a) and (b) shows the

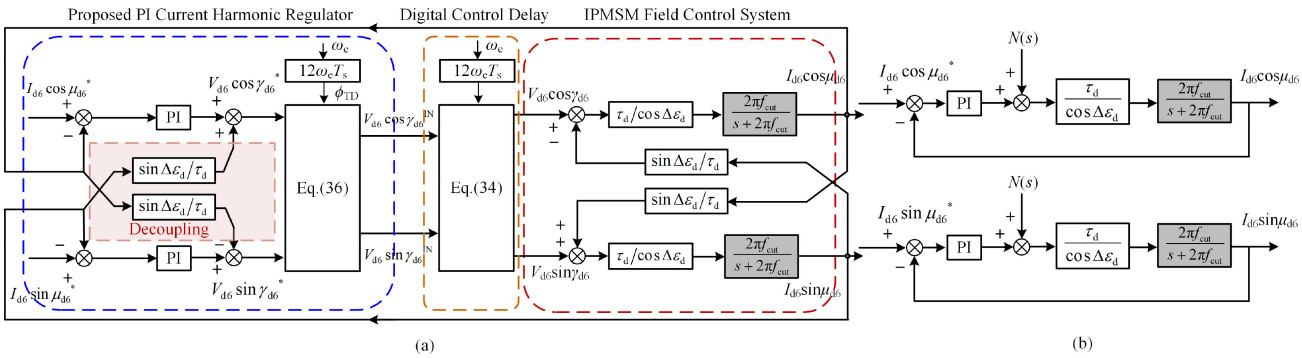

Fig. 8. Structural block diagram of d-axis current harmonic regulation system and equivalent control loop. (a) d-axis current harmonic regulation system. (b) Equivalent control loop.

structural block diagram and equivalent control loop diagram of the d-axis current harmonic regulation system, respectively. In current harmonic regulation system, IPMSM FOC system is the controlled object.

The PI transfer function of $I_{\mathrm{d6}}\cos\mu_{\mathrm{d6}}$ regulator can be expressed as

$$G_{\mathrm{PI}}(s) = k_{\mathrm{pd6\_cos}} + \frac{k_{\mathrm{id6\_cos}}}{s}. \tag{39}$$

Combined with Fig. 8(b) and (32), the open-loop transfer function of $I_{\mathrm{d6}}\cos\mu_{\mathrm{d6}}$ control loop can be obtained

$$G_{\mathrm{op}}(s) = \frac{2\pi f_{\mathrm{cut}} k_{\mathrm{pd\_cos}} s + 2\pi f_{\mathrm{cut}} k_{\mathrm{id\_cos}}}{\left(R + k_{\mathrm{pd}}\cos\phi_{\mathrm{TD}} - \frac{k_{\mathrm{id}}}{6\omega_{\mathrm{e}}}\sin\phi_{\mathrm{TD}}\right)(s^2 + 2\pi f_{\mathrm{cut}} s)} \tag{40}$$

where $k_{\mathrm{pd\_cos}}$ and $k_{\mathrm{id\_cos}}$ are the PI parameter of $I_{\mathrm{d6}}\cos\mu_{\mathrm{d6}}$ regulator; f_{cut} is the cutoff frequency of a FLPF for current harmonic characteristic quantities extraction.

In order to investigate the effect of $k_{\mathrm{pd\_cos}}$ and $k_{\mathrm{id\_cos}}$ on the regulation of $I_{\mathrm{d6}}\cos\mu_{\mathrm{d6}}$, the open-loop bode diagram and closed-loop unit step response curves of $I_{\mathrm{d6}}\cos\mu_{\mathrm{d6}}$ control loop with different $k_{\mathrm{pd\_cos}}$ and $k_{\mathrm{id\_cos}}$ at 1000 r/min are drawn, respectively, as shown in Figs. 9 and 10. The corresponding parameters of the IPMSM FOC system are shown in Table I.

As can be seen from the amplitude-frequency characteristic curve in Fig. 9, as the increase of $k_{\mathrm{pd\_cos}}$, the phase angle margin also increases, indicating that the stability of the system becomes better. It can also be seen from the closed-loop step response curve that a small $k_{\mathrm{pd\_cos}}$ will cause the shock of the current harmonic regulation system. With the increase of $k_{\mathrm{pd\_cos}}$, the system shock decreases and the system stability becomes stronger. Moreover, with the increase of $k_{\mathrm{pd\_cos}}$, the cutoff frequency of system increases, the system rapidity increases. But the adjustment time will increase. Therefore, when the system oscillates, $k_{\mathrm{pd\_cos}}$ should be increased, and when the system adjustment time is long, $k_{\mathrm{pd\_cos}}$ should be reduced. In the current several sets of $k_{\mathrm{pd\_cos}}$, 1.0 is the optimal.

Fig. 10 is the amplitude—frequency characteristic curve and closed-loop step response curve of $I_{\mathrm{d6}}\cos\mu_{\mathrm{d6}}$ control loop at different $k_{\mathrm{id\_cos}}$. As can be seen from amplitude–frequency characteristic curve, with the increases of $k_{\mathrm{id\_cos}}$, the slope, which is near the cutoff frequency, increases. So, the rapidity of the system increases. As can be seen from the closed-loop

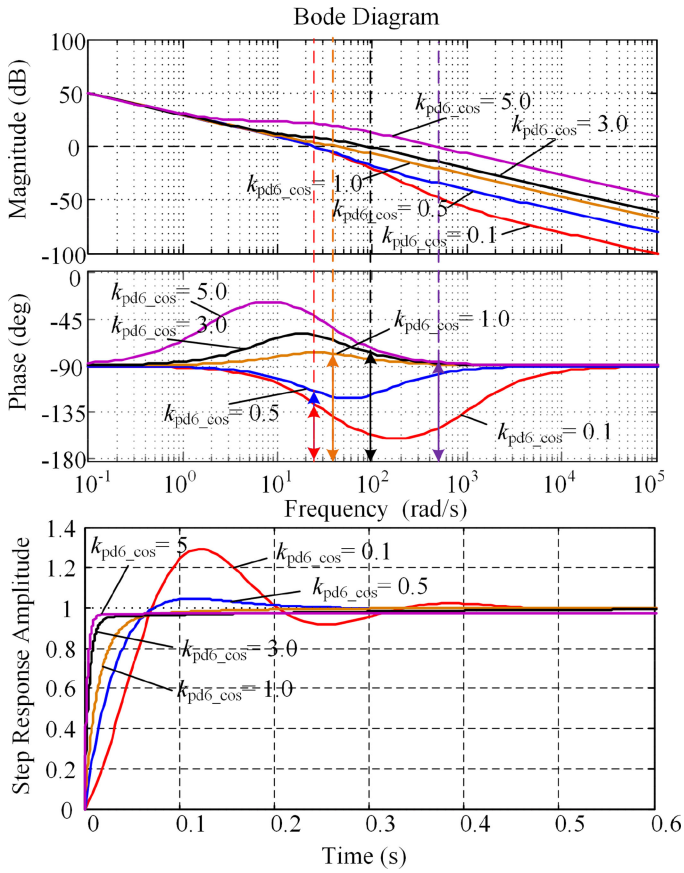

Fig. 9. Bode diagram and unit step response curve of $I_{\mathrm{d6}}\cos\mu_{\mathrm{d6}}$ control loop at different $k_{\mathrm{pd6\_cos}}$ and $k_{\mathrm{id6\_cos}} = 10.0$.

step response curve, with the increase of $k_{\mathrm{id\_cos}}$, the rise time of the system decreases and the rapidity of the system increases. Therefore, $k_{\mathrm{id\_cos}}$ should be increased when the rise time of the system is long.

IV. Simulation and Experimental Results

A. Simulation for Calculation Model of the Sixth D-Axis and Q-Axis Current Harmonics

Due to the influence of simulation step size, when the dead time is set in the simulation, it is difficult to accurately determine the specific value of d-axis and q-axis voltage harmonics induced

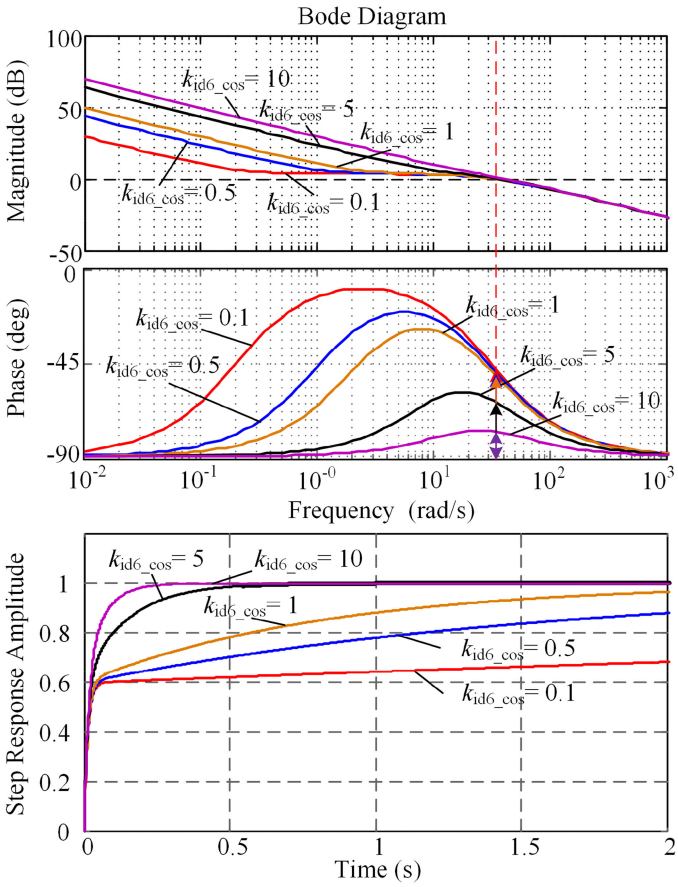

Fig. 10. Bode diagram and unit step response curve of $I_{d6}\cos\mu_{d6}$ control loop at different k_{id6_cos} and $k_{pd6\_cos} = 1.0$.

into the IPMSM FOC system. For simplicity, in order to verify the accuracy of the current harmonic calculation model proposed by this article, the simulation is built in MATLAB/Simulink in the absence of dead time. The parameters of IPMSM are given in Table I.

In the simulation, the torque reference is 72 N·m. Without setting the dead time of inverter, sixth voltage harmonics with amplitude of 5 and 10 V are added to the *d*-axis and *q*-axis current loops, respectively, and the speed is set to 500, 1000, 2000, and 3000 r/min. Then, the simulated *d*-axis and *q*-axis currents are analyzed by Fourier transform and the magnitudes of the sixth current harmonics are obtained. The results of Fourier analysis, the calculation formula proposed by this article [see(18)], and the traditional calculation formula [see(19)] are compared. The comparison results are shown in Fig. 11. It can be seen from the figure that the result calculated by (18) is close to the actual result, whereas the result calculated by (19) is far from the actual result. Furthermore, the calculation results without considering the digital control delay are compared. It can be found that without considering the digital control delay, the calculation results will deviate from the Fourier analysis results.

Through the aforementioned comparison, it can be seen that the current harmonic calculation model proposed by this article considers the influence of voltage harmonics output by *d*-axis and *q*-axis current controllers and digital control delay, so it has better accuracy than the traditional calculation method.

TABLE I
PARAMETERS OF IPMSM

Paramerters	Symbol	Value	Unit
Pairs of poles	n_p	4	--
Permanent magnet flux	λ_f	0.038749	Wb
Phase resistance	R	0.03	Ω
d-axis inductance	L_d	0.1049	mH
q-axis inductance	L_q	0.3453	mH
Rated speed	n	3000	r/min
Rated torque	T_N	72	Nm
Rated voltage	U_N	320	V
Control period	T_s	0.1	ms
Cut-off frequency	f_{cut}	5	Hz
Current loop bandwidth	f_N	300	Hz
Proportion of d-axis current controller	k_{pd}	$2\pi f_N L_d$	--
Integration of d-axis current controller	k_{pi}	$2\pi f_N R$	--

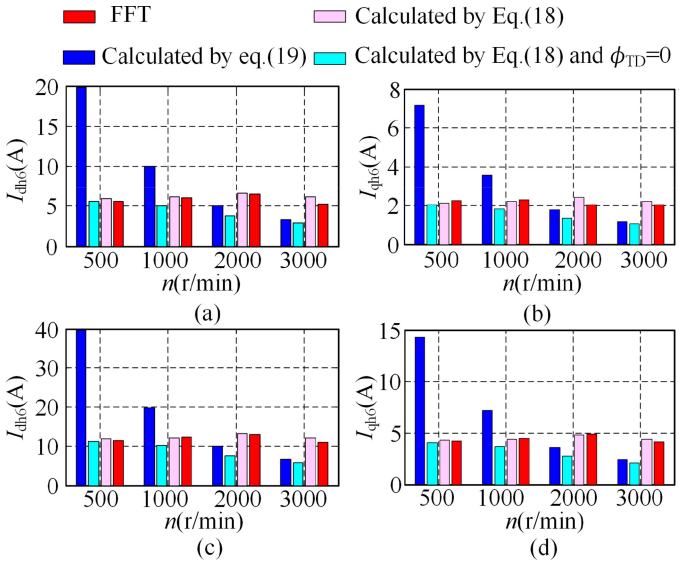

Fig. 11. Comparison of sixth *d*-axis, *q*-axis harmonic current amplitudes are calculated by proposed calculation method and traditional calculation method. (a) $V_{dh6} = 5$ V. (b) $V_{qh6} = 5$ V. (c) $V_{dh6} = 10$ V. (d) $V_{qh6} = 10$ V.

B. Simulate Verification for PI Parameter Design of Proposed Current Harmonic Regulators

In order to verify the design guidelines of current harmonic regulator parameters designed in this article, the following simulation verification is carried out. The dead time of inverter is set to 2.6 μs in simulation. For comparison with Figs. 9 and 10, the current harmonic regulator of *d*-axis current harmonic characteristic quantity ($I_{d6}\cos\mu_{d6}$) is also taken as an example. In simulation, the speed of IPMSM is 1000 r/min, the torque reference is 30 N·m, and the reference of $I_{d6}\cos\mu_{d6}$ is set to 0. When k_{id_cos} is set as 10.0, k_{pd_cos} is set as 0.1, 0.5, 1.0, 3.0, and

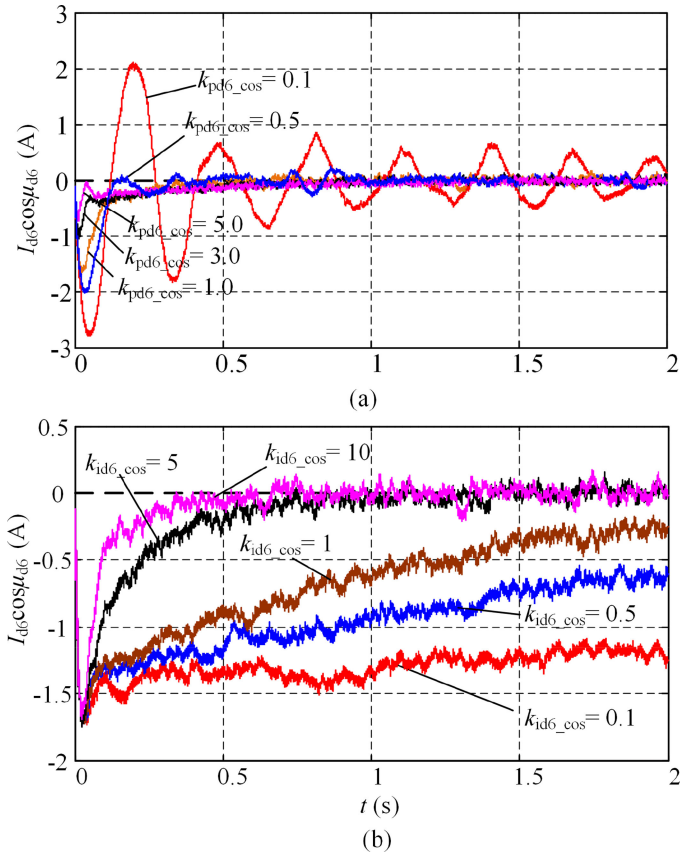

Fig. 12. Step response simulation waveform of $I_{d6}\cos\mu_{d6}$ under different PI current harmonic regulator parameters. (a) $k_{id\_cos} = 10.0$, $k_{pd\_cos} = 0.1$, 0.5, 1.0, 3.0, 5.0. (b) $k_{pd\_cos} = 1.0$, $k_{id\_cos} = 0.1$, 0.5, 1.0, 5.0, 10.0.

5.0, successively. Step response waveform of $I_{d6}\cos\mu_{d6}$ under different k_{pd_cos} is shown in Fig. 12(a). Then, when k_{pd_cos} is set as 1.0, k_{id_cos} is set as 0.1, 0.5, 1.0, 5.0, and 10.0, successively. Step response waveform of $I_{d6}\cos\mu_{d6}$ under different k_{id_cos} is shown in Fig. 12(b).

As can be seen from Fig. 12, a small k_{pd_cos} will cause the shock of the current harmonic regulation system. With the increase of k_{pd_cos}, the system shock decreases; with the increase of k_{pd_cos}, the rise time decreases and the adjustment time increases. Increasing k_{id_cos} is beneficial to improve the rapidity of the system. The simulation results are consistent with the closed-loop step response curves in Figs. 9 and 10.

C. Experimental Verification of Proposed Current Harmonic Characteristic Quantities Extraction Method

To verify the feasibility of the proposed methods, an experimental system shown in Fig. 13 is set up. The experimental test bench consists of a dynamometer, a dc power supply, an inverter, and a control unit, which is built by DSP(TMS320F28335). Besides, the dead time of inverter is set as 2.6 μs. The sampling frequency and carrier frequency of the control system are both 10 kHz. The vibration on the motor shaft is measured by a noncontact rotating laser vibrometer (RLV-5500).

Figs. 14 and 15 show the experimental waveforms of the traditional current harmonic extraction method based on MSRFT

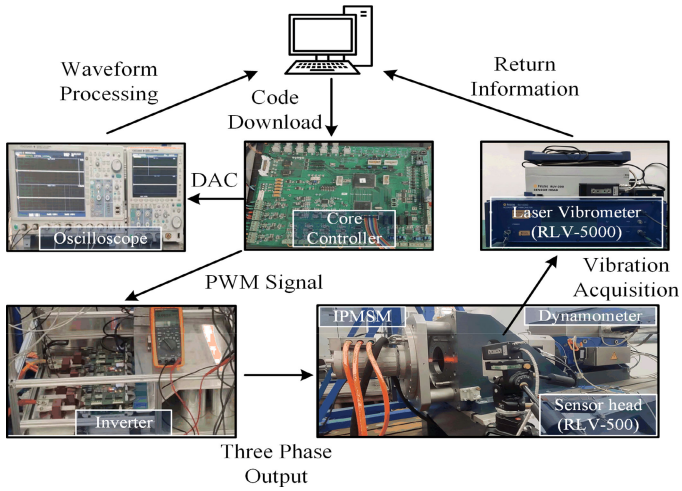

Fig. 13. Experimental system.

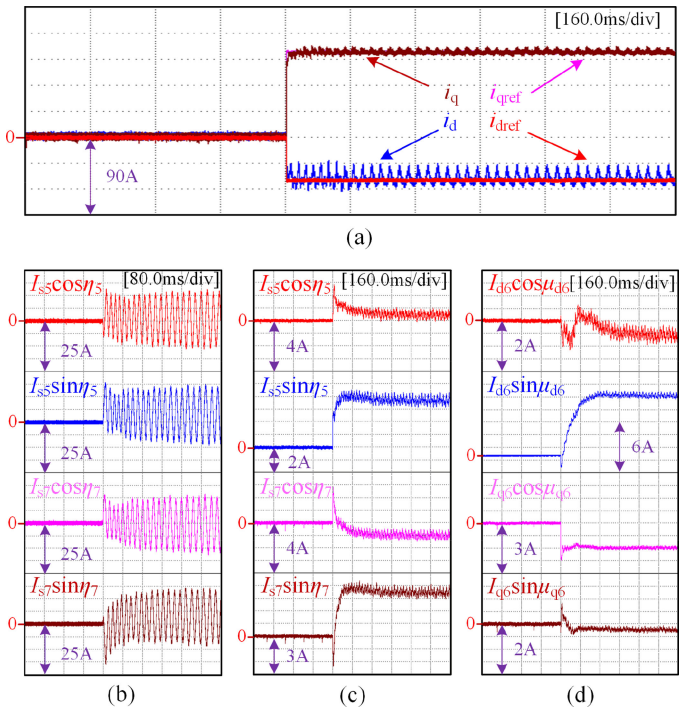

Fig. 14. Extraction results of current harmonic at 100 r/min, $T_{e\_ref} = 30$ N·m. (a) d-axis and q-axis currents. (b) Fifth, seventh current harmonic characteristic quantities are extracted by the traditional method. (c) Fifth, seventh current harmonic characteristic quantities are extracted by the proposed method. (d) Sixth current harmonic characteristic quantities are extracted by the proposed method.

and the proposed d-axis and q-axis current harmonic extraction method based on MSRFT at 100 and 3000 r/min, respectively. It can be seen from them that the fifth and seventh current harmonics characteristic quantities extracted by the traditional current harmonic extraction method contain ac components, which is especially serious at low speed. The proposed current harmonic extraction method can extract the current harmonic characteristic quantities well at both low speed and high speed.

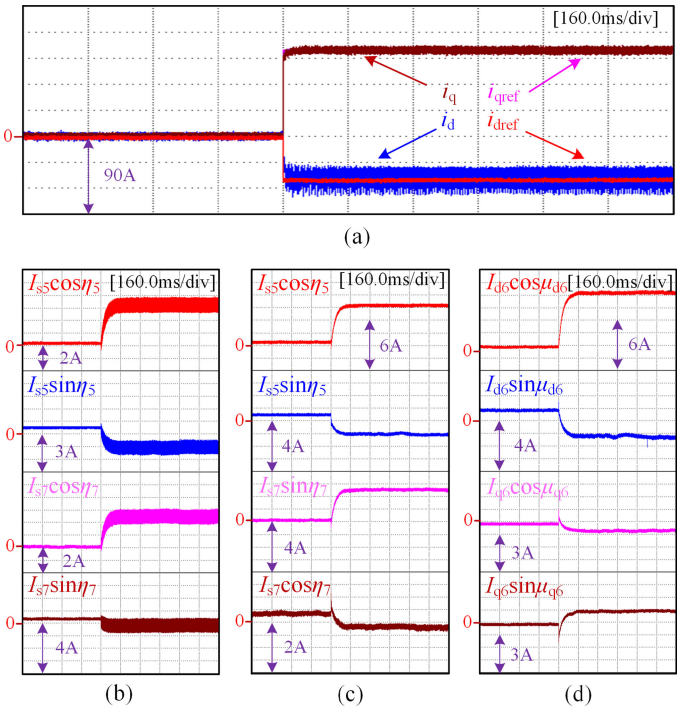

Fig. 15. Extraction results of current harmonic at 3000 r/min, T_{e_ref} = 30 N·m. (a) *d*-axis and *q*-axis currents. (b) Fifth, seventh current harmonic characteristic quantities are extracted by the traditional method. (c) Fifth, seventh current harmonic characteristic quantities are extracted by the proposed method. (d) Sixth current harmonic characteristic quantities are extracted by the proposed method.

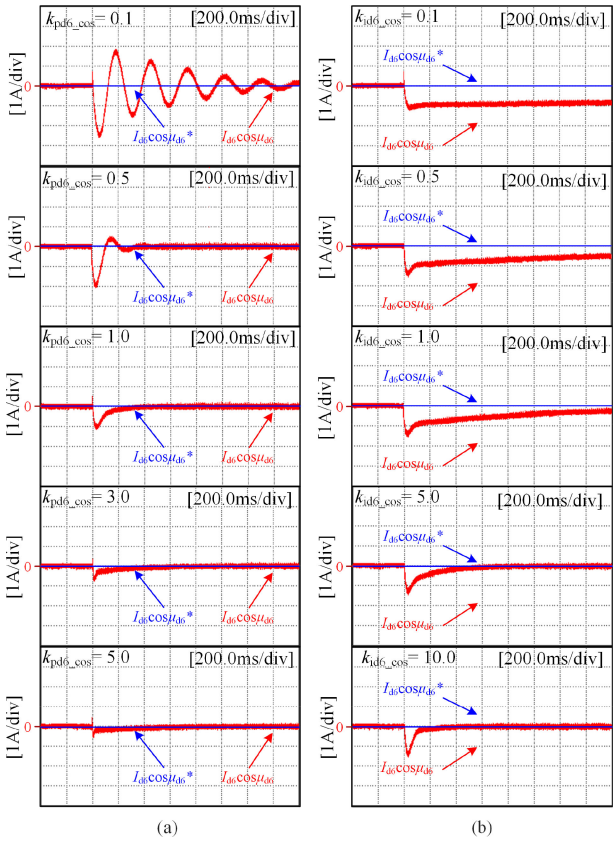

Fig. 16. Step response experimental waveforms of $I_{d6}\cos\mu_{d6}$ under different PI current harmonic regulator parameters. (a) k_{id_cos} = 10.0, k_{pd_cos} = 0.1, 0.5, 1.0, 3.0, 5.0. (b) k_{pd_cos} = 1.0, k_{id_cos} = 0.1, 0.5, 1, 5, 10.

Therefore, the proposed method improves the application performance and accuracy of current harmonic extraction method based on MSRFT in motor control system.

D. Experimental Verification of Proposed Current Harmonic Regulator Based on Unified Coordinate Frame

Fig. 16 is the experimental verification results for PI parameter design of proposed current harmonic regulators. The experimental conditions are consistent with the simulation conditions in Section IV-B. As can be seen from Fig. 16, a small k_{pd_cos} will cause the shock of the current harmonic regulation system. With the increase of k_{pd_cos}, the system shock decreases; with the increase of k_{pd_cos}, the rise time decreases and the adjustment time increases. Increasing k_{id_cos} is beneficial to improve the rapidity of the system. The experimental results are consistent with the simulation results in Fig. 12. Therefore, the parameter design principle given in this article can be a good guide to the PI parameter design of proposed current harmonic regulator based on unified coordinate frame.

In order to verify the control effect of the proposed current harmonic regulator on current harmonic, the following experiments are carried out. The current harmonic extraction method used in this experimental part is proposed by this article. Because the permanent magnet flux of IPMSM used in the experiment does not contain fifth and seventh harmonics, in order to reduce torque ripple and motor loss, the current harmonic should be controlled to zero.

When the motor speed is 100 r/min and the torque changes from 0 to 30 N·m and then to 72 N·m, the current harmonic characteristic quantities of IPMSM FOC system without harmonic current regulators are shown in Fig. 17(a). The control effect of the traditional PI current harmonic regulator on the current harmonic is shown in Fig. 17(b). It can be seen from the figure that under this working condition, $I_{s7}\sin\eta_7$ are out of control. So, traditional PI current harmonic regulator is difficult to effectively control the current harmonic. Fig. 17(d) shows the control effect of proposed PI current harmonic regulator based on unified coordinate frame on current harmonic. It can be seen that proposed PI current harmonic regulator based on unified coordinate frame can control the current harmonic effectively.

When the motor speed is 3000 r/min and the torque changes from 0 to 30 N·m and then to 72 N·m, the control effect of the traditional PI current harmonic regulator on the current harmonic is shown in Fig. 18(b). It can be seen from the figure that under this working condition, $I_{s5}\cos\eta_5$, $I_{s5}\sin\eta_5$, $I_{s7}\cos\eta_7$, and $I_{s7}\sin\eta_7$ are all out of control. So, traditional PI current harmonic regulator is difficult to effectively control the current harmonic at high speed. Fig. 18(d) shows the control effect of proposed PI current harmonic regulator based on unified coordinate frame on current harmonic. It can be seen that proposed PI current harmonic regulator based on unified coordinate frame can control the current harmonic, effectively.

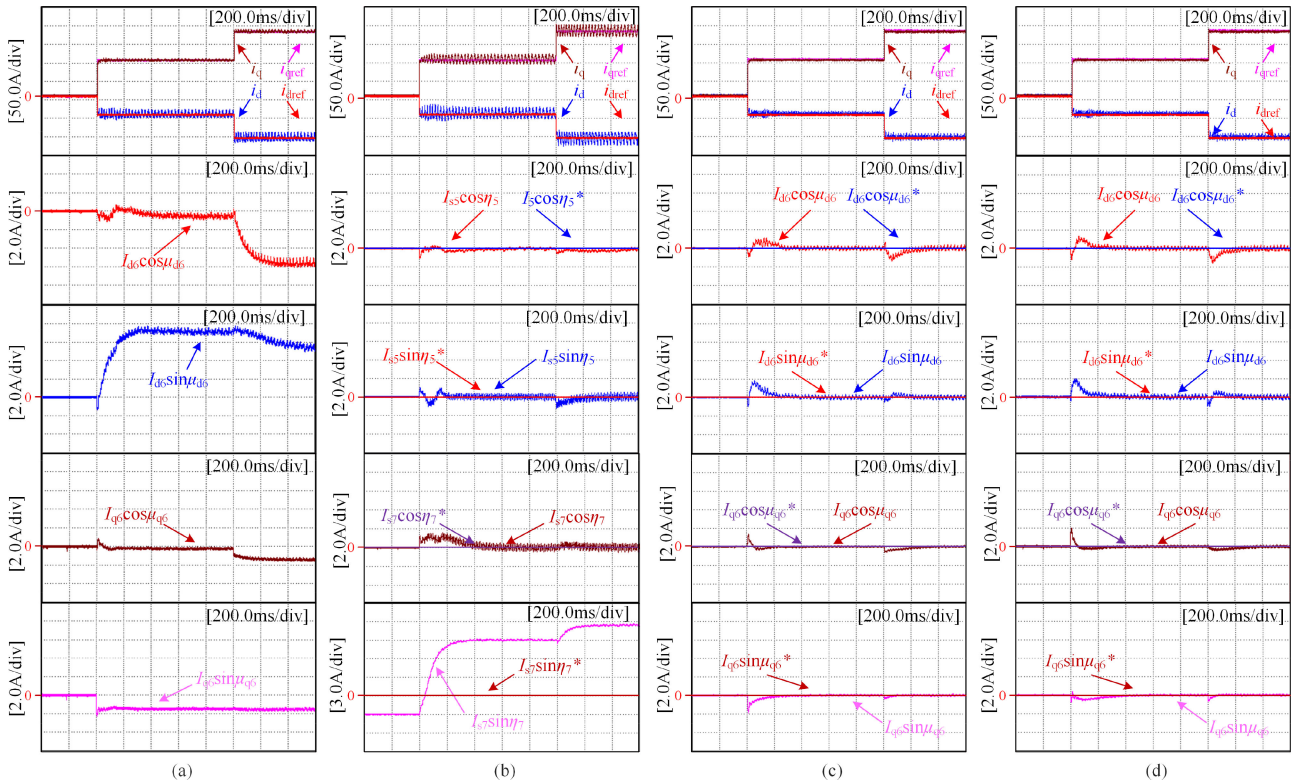

Fig. 17. Experimental results of current harmonic regulator at 100 r/min, $T_{\mathrm{e\_ref}} = 3072$ N·m. (a) Without harmonic current regulator. (b) Traditional PI current harmonic regulator. (c) Proposed PI current harmonic regulator based on unified coordinate frame unconsidering ϕ_{TD}. (d) Proposed PI current harmonic regulator based on unified coordinate frame.

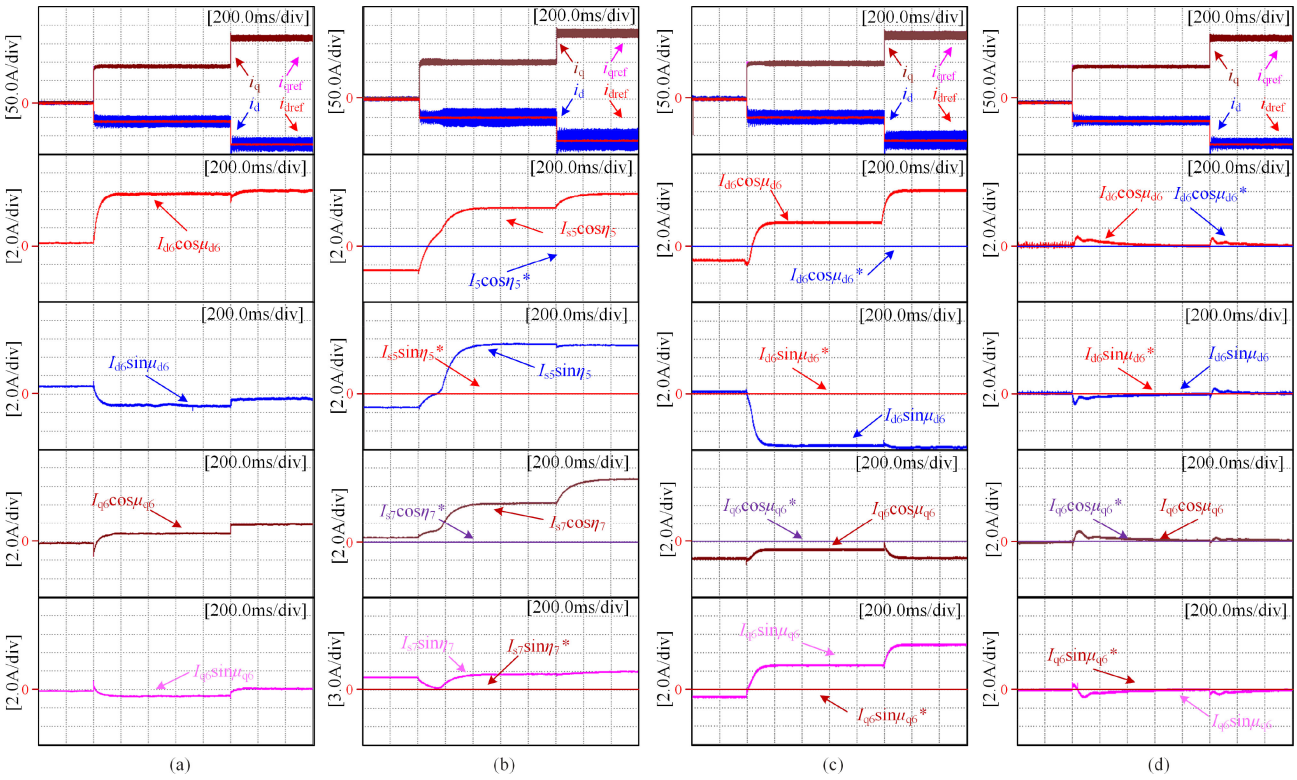

Fig. 18. Experimental results of current harmonic regulator at 3000 r/min, $T_{\mathrm{e\_ref}} = 3072$ N·m. (a) Without harmonic current regulator. (b) Traditional PI current harmonic regulator. (c) Proposed PI current harmonic regulator based on unified coordinate frame unconsidering ϕ_{TD}. (d) Proposed PI current harmonic regulator based on unified coordinate frame.

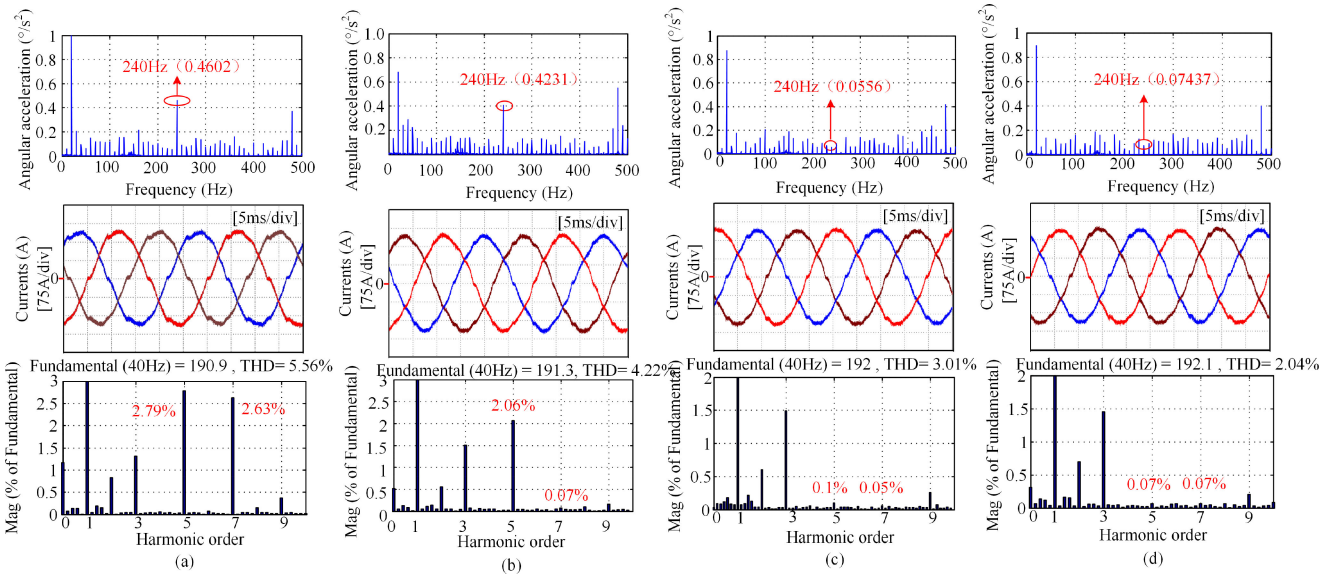

Fig. 19. Field-oriented control results of angular acceleration and currents at 600 r/min. (a) Without current harmonic regulator. (b) With traditional PI current harmonic regulator. (c) With proposed PI current harmonic regulator based on unified coordinate frame unconsidering ϕ_{TD}. (d) With proposed PI current harmonic regulator based on unified coordinate frame considering ϕ_{TD}.

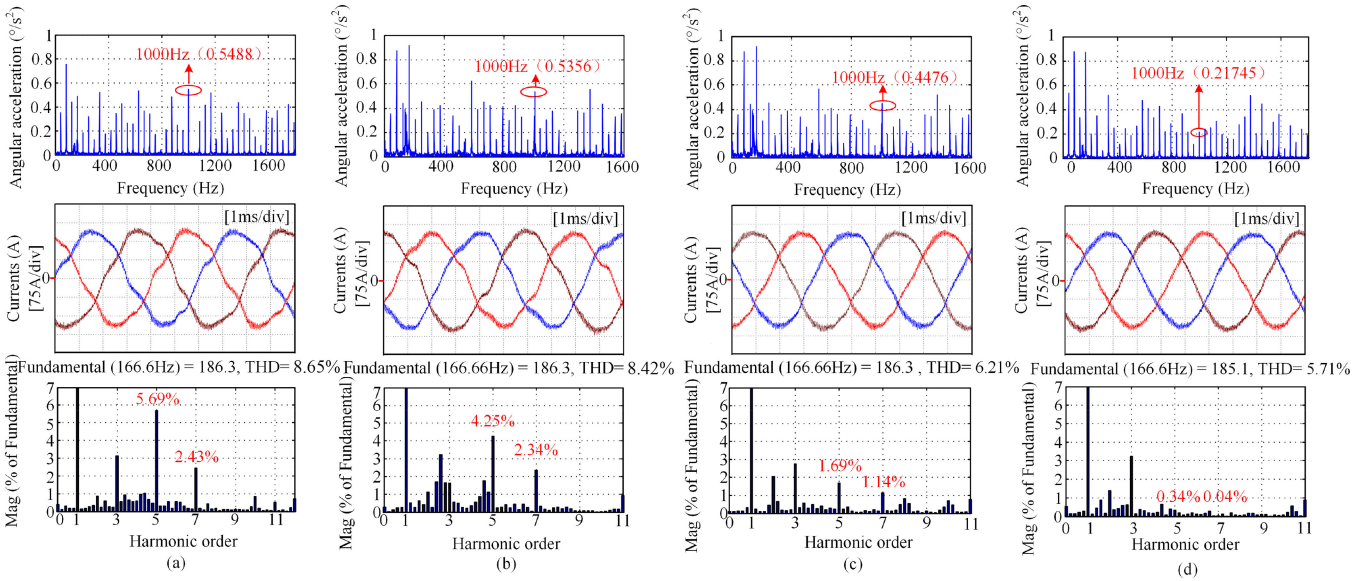

Fig. 20. Field-oriented control results of angular acceleration and currents at 2500 r/min. (a) Without current harmonic regulator. (b) With traditional PI current harmonic regulator. (c) With proposed PI current harmonic regulator based on unified coordinate frame unconsidering ϕ_{TD}. (d) With proposed PI current harmonic regulator based on unified coordinate frame considering ϕ_{TD}.

By comparing Fig. 17(b) and Fig. 18(b), it can be seen that under different working conditions, the uncontrolled current harmonics in the traditional PI current harmonic regulator will change, thus increasing the control uncertainty. Comparing Fig. 17(c) with Fig. 18(c), it can be seen that if the initial phase of the voltage harmonic output by the current harmonic regulator is not compensated, the control of the current harmonic will fail at high speed.

In order to further verify the improvement effect of the proposed current harmonic regulator on motor torque ripple, the following experiments are carried out. The vibration on the motor shaft is measured by a noncontact rotating laser vibrometer (RLV-5500). The vibration meter is composed of sensor head (RLV-500) and signal processor (RLV-5000). The sensor sends out two parallel laser beams to hit IPMSM shaft. The returned laser beam is processed by a signal processor. Finally, the angular acceleration amplitude at different frequencies is observed by the host computer, so as to reflect the ripple of torque.

Fig. 19 shows the three-phase current waveforms, phase current Fourier analysis results, and vibration spectrum on the motor shaft under different control strategies when the motor speed is 600 r/min. Fig. 19(a) shows the results of field-oriented control

without current harmonic regulator. Fig. 19(b) shows the results of field-oriented control with traditional PI current harmonic regulator. Fig. 19(c) shows the results of field-oriented control with proposed PI current harmonic regulator based on unified coordinate frame unconsidering ϕ_{TD}. Fig. 19(d) shows the results of field-oriented control with proposed PI current harmonic regulator based on unified coordinate frame considering ϕ_{TD}. Similarly, Fig. 20 shows the three-phase current waveforms, phase current Fourier analysis results, and vibration spectrum on the motor shaft under different control strategies when the motor speed is 2500 r/min.

By comparing Fig. 19(a), (b), and (d) and Fig. 20(a), (b), and (d), it can be seen that under the traditional PI current harmonic regulator, the current harmonic is difficult to effectively follow the references (0), and the vibration on the motor shaft is difficult to be effectively reduced. The current harmonic regulator based on unified coordinate frame proposed by this article can effectively reduce the vibration on the motor shaft. In other words, the motor torque ripple is effectively reduced. Comparing Fig. 19(c) with Fig. 20(c), it can be seen that if the initial phase of the voltage harmonic output by the current harmonic regulator is not compensated, the control of the current harmonic will fail at high speed. The vibration on the motor is difficult to be effectively reduced.

The aforementioned experiments show that the traditional PI current harmonic regulator is difficult to effectively control the current harmonic, and the PI current harmonic regulator based on the unified coordinate frame designed by this article can effectively control the current harmonic. Digital control delay will affect the initial phase angle of voltage harmonics output by current harmonic regulator, and then affect the control of current harmonic. Therefore, it is necessary to compensate the initial phase angle of voltage harmonics in the design of current harmonic regulator. Through the effective control of current harmonics, the torque ripple of the motor can be reduced.

V. Conclusion

In this article, the mathematical model of d-axis and q-axis current harmonic of IPMSM and the control of current harmonic are studied. The work content is mainly reflected in the following aspects.

1) The influence of voltage harmonics generated by d-axis and q-axis current controllers on current harmonics in field-oriented control system is fully considered and the influence of digital control delay on the initial phase angle of voltage harmonics output by d-axis and q-axis current controllers is also analyzed for the first time. On this basis, an accurate calculation model of d-axis and q-axis current harmonics in field-oriented control system is derived.
2) An improved current harmonic extraction method based on MSRFT is proposed. The application performance and accuracy of current harmonic extraction method based on MSRFT in motor control field are improved.
3) Based on the established current harmonic calculation model, a PI current harmonic regulator based on unified coordinate frame is designed. This current harmonic regulator includes current harmonic decoupling and voltage harmonic initial phase angle compensation. Compared with the traditional PI current harmonic regulator, the current harmonic regulator proposed by this article can realize the effective control of current harmonic.

The current harmonic regulator designed in this article can be used for torque ripple suppression, current harmonic suppression, sensorless control of high-frequency signal injection, and other occasions that need accurate control of current harmonic. It provides a good current harmonic control method.

References

[1] L. Wang, Z. Zhu, H. Bin, and L. Gong, "Current harmonics suppression strategy for PMSM with nonsinusoidal back-EMF based on adaptive linear neuron method," *IEEE Trans. Ind. Electron.*, vol. 67, no. 11, pp. 9164–9173, Nov. 2020.

[2] G. Liu, B. Chen, K. Wang, and X. Song, "Selective current harmonic suppression for high-speed PMSM based on high-precision harmonic detection method," *IEEE Trans. Ind. Informat.*, vol. 15, no. 6, pp. 3457–3468, Jun. 2019.

[3] A. Lewicki, "Dead-time effect compensation based on additional phase current measurements," *IEEE Trans. Ind. Electron.*, vol. 62, no. 7, pp. 4078–4085, Jul. 2015.

[4] D. Park and K. Kim, "Parameter-independent online compensation scheme for dead time and inverter nonlinearity in IPMSM drive through waveform analysis," *IEEE Trans. Ind. Electron.*, vol. 61, no. 2, pp. 701–707, Feb. 2014.

[5] T. Qiu, X. Wen, and F. Zhao, "Adaptive-linear-neuron-based dead-time effects compensation scheme for PMSM drives," *IEEE Trans. Power Electron.*, vol. 31, no. 3, pp. 2530–2538, Mar. 2016.

[6] Z. Wu, K. Ding, Z. Yang, and G. He, "Analytical prediction and minimization of dead-time related harmonics in PMSM," *IEEE Trans. Ind. Electron.*, vol. 68, no. 9, pp. 7736–7746, Sep. 2021.

[7] Z. Wu *et al.*, "Dead-time compensation based on a modified multiple complex coefficient filter for permanent magnet synchronous machine drives," *IEEE Trans. Power Electron.*, vol. 36, no. 11, pp. 12979–12988, Nov. 2021.

[8] C. Lai, G. Feng, K. Mukhrejee, V. Loukanov, and Narayan C. Kar, "Torque ripple modeling and minimization for interior PMSM considering magnetic saturation," *IEEE Trans. Power Electron.*, vol. 33, no. 3, pp. 2417–2429, Mar. 2021.

[9] B. Zheng, J. Bin, Y. Xu, X. Lang, and G. Yu, "Torque ripple suppression based on optimal harmonic current injection in dual three-phase PMSMs under magnetic saturation," *IEEE Trans. Ind. Electron.*, vol. 69, no. 6, pp. 5398–5408, Jun. 2022.

[10] J. Qu, J. Iatskevich, C. Zhang, and S. Zhang, "Torque ripple reduction method for permanent magnet synchronous machine drives with novel harmonic current control," *IEEE Trans. Energy Convers.*, vol. 36, no. 3, pp. 2502–2513, Sep. 2021.

[11] Z. Tang and B. Akin, "A new LMS algorithm based deadtime compensation method for PMSM FOC drives," *IEEE Trans. Ind. Appl.*, vol. 54, no. 6, pp. 6472–6484, Nov./Dec. 2018.

[12] P. Yi, X. Wang, and Z. Sun, "Instantaneous harmonic decomposition technique for three-phase current based on multiple reference coordinates," *IET Elect. Power Appl.*, vol. 12, no. 4, pp. 547–556, Feb. 2018.

[13] G. Feng, C. Lai, W. Li, Z. Li, and N. C. Kar, "Dual reference frame based current harmonic minimization for dual three-phase PMSM considering inverter voltage limit," *IEEE Trans. Power Electron.*, vol. 36, no. 7, pp. 8055–8066, Jul. 2021.

[14] G. Feng, C. Lai, J. Tian, and N. C. Kar, "Multiple reference frame based torque ripple minimization for PMSM drive under both steady-state and transient conditions," *IEEE Trans. Power Electron.*, vol. 34, no. 7, pp. 6685–6696, Jul. 2019.

[15] W. Wang, C. Liu, S. Liu, Z. Song, H. Zhao, and B. Dai, "Current harmonic suppression for permanent-magnet synchronous motor based on Chebyshev filter and PI controller," *IEEE Trans. Magn.*, vol. 57, no. 2, Feb. 2021, Art. no. 8201406.

[16] Z. Tang and B. Akin, "Suppression of dead-time distortion through revised repetitive controller in PMSM drives," *IEEE Trans. Energy Convers.*, vol. 32, no. 3, pp. 918–930, Sep. 2017.
[17] W. Deng, C. Xia, Y. Yan, Q. Geng, and T. Shi, "Online multiparameter identification of surface-mounted PMSM considering inverter disturbance voltage," *IEEE Trans. Energy Convers.*, vol. 32, no. 1, pp. 202–212, Mar. 2017.
[18] G. Escobar, P. G. Hernandez-Briones, P. R. Martinez, M. Hernandez-Gomez, and R. E. Torres-Olguin, "A repetitive-based controller for the compensation of 6l±1 harmonic components," *IEEE Trans. Ind. Electron.*, vol. 55, no. 8, pp. 3150–3158, Aug. 2008.
[19] H. Kim, Y. Han, K. Lee, and S. Bhattacharya, "A sinusoidal current control strategy based on harmonic voltage injection for harmonic loss reduction of PMSMs with non-sinusoidal back-EMF," *IEEE Trans. Ind. Appl.*, vol. 56, no. 6, pp. 7032–7043, Nov./Dec. 2020.
[20] B. H. Bae and S. K. Sul, "A compensation method for time delay of full-digital synchronous frame current regulator of PWM AC drives," *IEEE Trans. Ind. Appl.*, vol. 39, no. 3, pp. 802–810, Mar.–Jun. 2003.

Zhiwei Chen was born in Pingdingshan, China, in 1994. He received the B.S. degree in electrical engineering from the China University of Mining and Technology, Xuzhou, China, in 2017. He is currently working toward the Ph.D. degree in electrical engineering with the School of Electrical and Information Engineering, Tianjin University, Tianjin, China.

His research interests include electrical machines, motor drives, and power electronics.

Tingna Shi (Member, IEEE) was born in Yuyao, China, in 1969. She received the B.S. and M.S. degrees in electrical engineering from Zhejiang University, Hangzhou, China, in 1991 and 1996, respectively, and the Ph.D. degree in electrical engineering from Tianjin University, Tianjin, China, in 2009.

She is currently a Professor with the College of Electrical Engineering, Zhejiang University. Her current research interests include electrical machines and their control systems, power electronics, and electric drives.

Zhichen Lin was born in Shandong, China, in 1993. He received the B.S. degree in electrical engineering from Dalian Maritime University, Dalian, China, in 2016, and the Ph.D. degree in electrical engineering from Tianjin University, Tianjin, China, in 2021.

He is currently a Postdoctoral Researcher with the College of Electrical Engineering, Zhejiang University, Zhejiang, China. His research interests include electrical machines, motor drives, and power electronics.

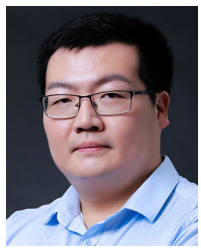

Zhiqiang Wang (Member, IEEE) was born in Tianjin, China, in 1984. He received the B.S. degree in electrical engineering from the Hebei University of Technology, Tianjin, China, in 2006, and the M.S. and Ph.D. degrees in electrical engineering from Tianjin University, Tianjin, China, in 2008 and 2012, respectively.

He is currently an Associate Professor with the School of Artificial Intelligence, Tiangong University, Tianjin, China. His research interests include power electronics technology and intelligent control of motor systems.

Xin Gu (Member, IEEE) was born in Tianjin, China, in 1980. He received the B.S., M.S., and Ph.D. degrees in electrical engineering from Tianjin University, Tianjin, China, in 2003, 2006, and 2010, respectively.

He joined Tiangong University, Tianjin, China, as a Lecturer in 2010. He is currently a Professor with the School of Electrical Engineering, and also with the National Local Joint Engineering Research Center of Electric Machine System Design and Manufacturing, China. His research interests include permanent magnet synchronous machines and their control systems.